Rheology of Planetary Lithosphere and the Style of Tectonics

Figure 9.1. Log–log plot of strain rate as a function of differential stress, illustrating the strength of coarse-grained polycrystalline ice relative to that of single crystals of ice oriented for slip on the basal plane and single crystals of ice oriented for slip on non-basal planes. Note that the differential stress required to deform polycrystalline samples at a given strain rate lies between the values for slip on the hard and easy slip systems in ice. Comparison of the slopes, that is, the stress exponent n, in Equation (9.6), of these three lines suggests that slip on non-basal systems controls the rate of deformation, while the relative positions of the lines indicates that basal slip contributes significantly to flow. Modified from Goldsby and Kohlstedt (2001).

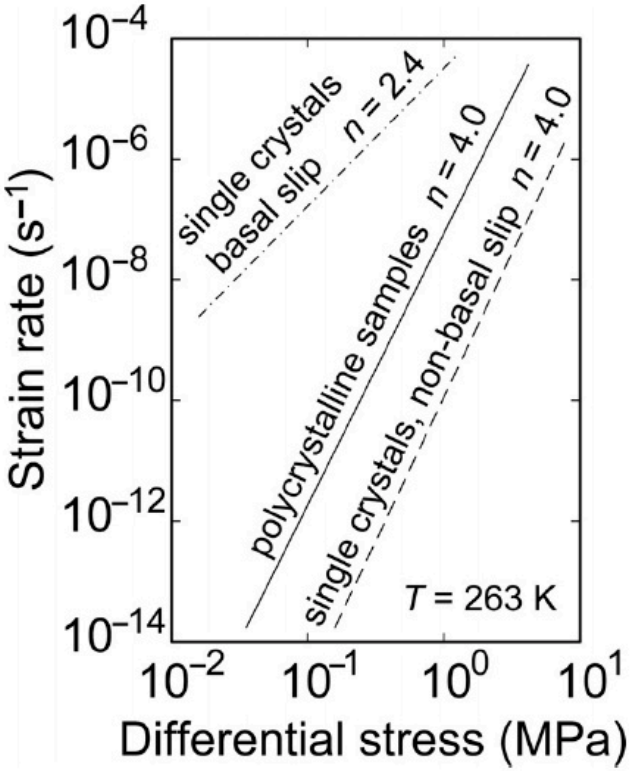

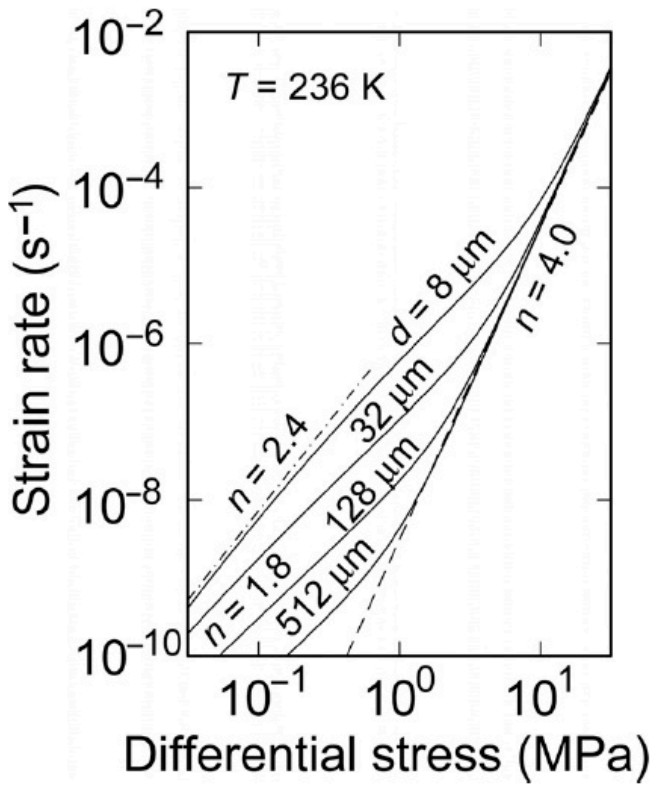

Figure 9.2. Log–log plot of viscosity as a function of differential stress for fine-grained polycrystalline ice with grain sizes of 8, 32, 128, and 512 μm. The flow law for coarse-grained ice deforming in the dislocation creep regime is indicated by the dashed line of slope $n = 4.0$, while the flow law for single crystals of ice oriented for slip on the basal plane is included as a dot-dashed line of slope $n = 2.4$. Between these two bounds, polycrystalline ice flows by grain boundary sliding accommodated by dislocation movement in the dislocation – grain boundary sliding regime characterized by a slope of $n = 1.8$.

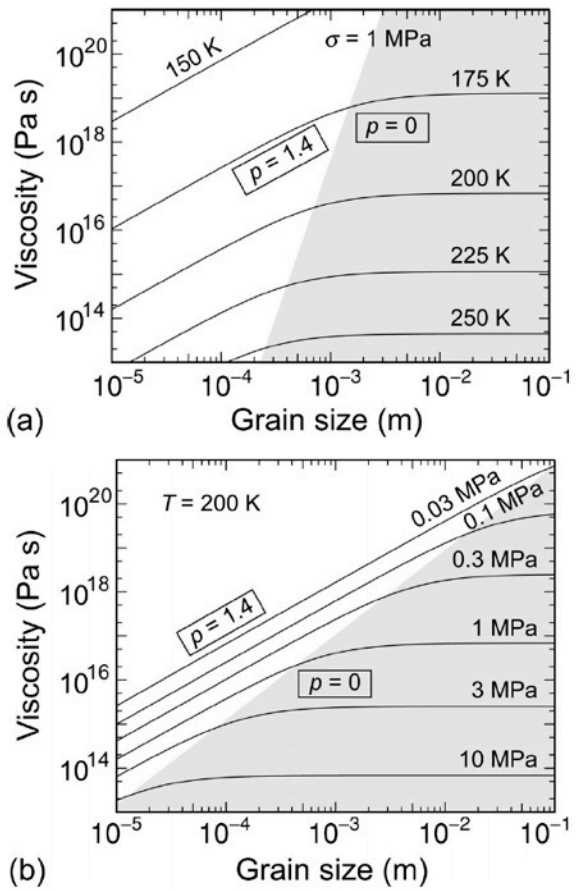

Figure 9.3. Log–log plots of viscosity as a function of grain size at (a) fixed differential stress of 1 MPa and (b) fixed temperature of 200 K. Dislocation creep dominates the viscosity at large grain sizes (shaded regions on the right of (a) and (b)), while dislocation – grain boundary sliding creep dominates at smaller grain sizes. Strain rate is independent of grain size ($p = 0$) in the former regime, while strain rate increases with decreasing grain size in the latter regime ($p = 1.4$). In (a), the transition between the two regimes occurs at smaller grain size with increasing temperature. In (b), the transition between the two regimes occurs at smaller grain size with increasing differential stress.

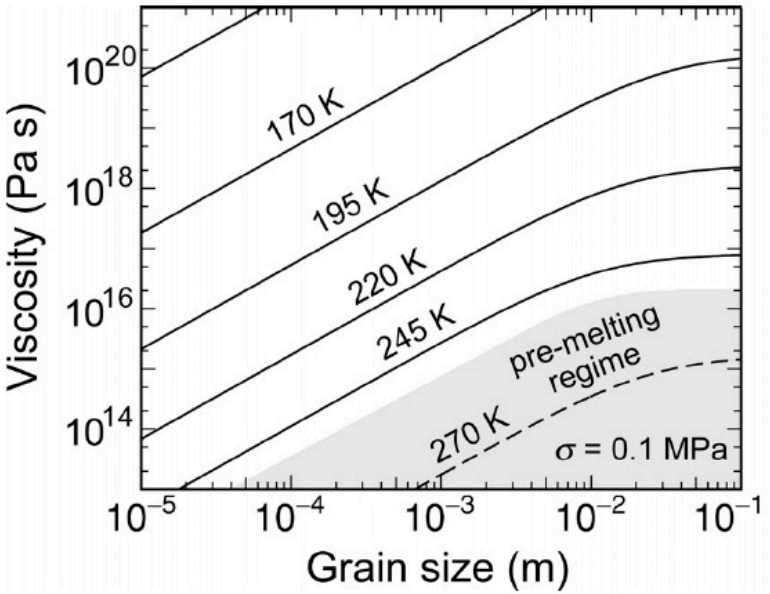

Figure 9.4. Log–log plot of strain rate as a function of grain size at a constant differential stress of 0.1 MPa for temperatures both below and above the pre-melting temperature of ~255 K. The temperature interval between constant-temperature curves is 25 K. With increasing temperature between 170 and 245 K, the contours become progressively closer. However, the spacing between the curve for 245 K and the curve for 270 K is significantly wider than that between the curves for 220 K and 245 K, reflecting the marked increase in activation energy from ~50 to ~180 kJ/mol in crossing the pre-melting point.

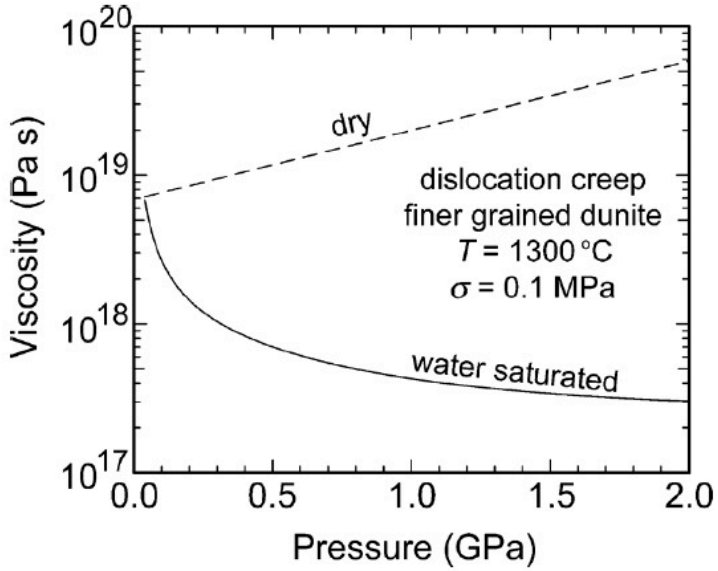

Figure 9.11. Semi-log plot of viscosity versus pressure for dunite in the dislocation creep regime. Under anhydrous (dry) conditions, viscosity increases with increasing pressure based on an exponential dependence of strain rate on pressure, Equations (9.5) and (9.6). Under hydrous (wet) conditions, viscosity decreases with increasing pressure due to the approximately linear dependence of strain rate on water fugacity, Equation (9.13b), since water fugacity increases with increasing pressure under water-saturated conditions (e.g., Pitzer and Sterner, 1994). This implicit effect of water fugacity on viscosity with increasing pressure is offset to some degree by the explicit exponential increase in viscosity with increasing pressure in Equation (9.13b).

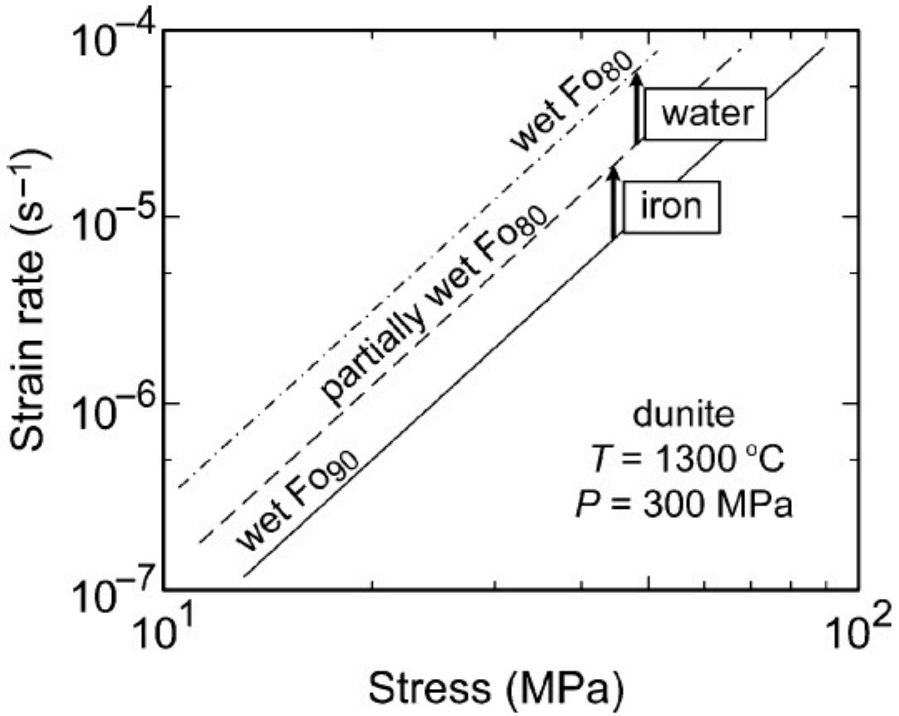

Figure 9.13. Log–log plot of strain rate versus differential stress illustrating the effect on creep rate behavior of increasing iron content in olivine. Based on Figure 9.12, at a given stress, the strain rate increases as iron content increases. In addition, water solubility increases with increasing iron content, thus further increasing the strain rate.

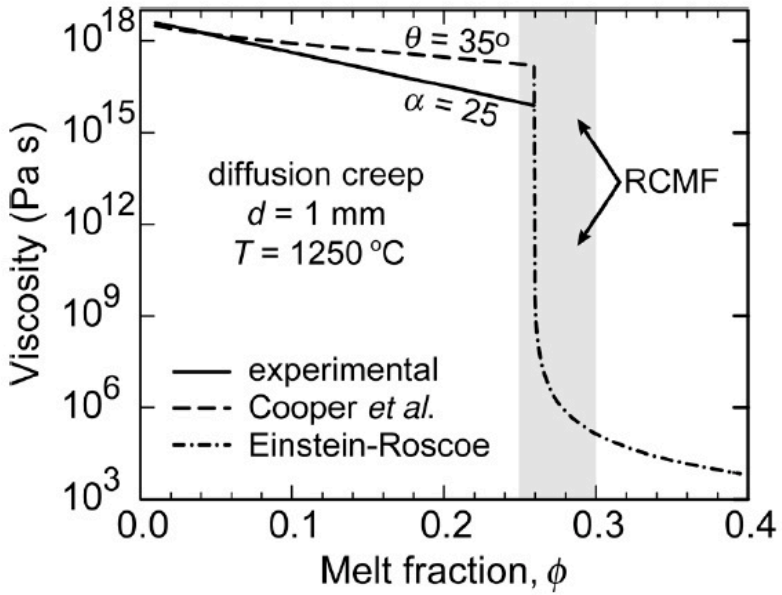

Figure 9.17. Semi-log plot of viscosity as a function of melt fraction for the diffusion creep regime. The dashed line is based on Equations (9.31) and (9.32) for $\theta = 35°$. The solid line is an empirical fit of experimental data to Equation (9.34) with $\alpha = 25$. The dot-dashed line is an extrapolation to higher melt fractions using the Einstein-Roscoe relationship in Equation (9.35). The shaded region identifies the rheologically critical melt fraction for the olivine plus basalt system based on experiments by Scott and Kohlstedt (2006).

Figure 9.5. Strength envelope plotting rock strength as a function of depth in the Earth for typical oceanic lithosphere deforming at a strain rate of 10^{-14} s^{-1}. An oceanic geotherm from Turcotte and Schubert (1982) for 60 m.y. lithosphere is assumed. The basaltic composition crust of 6 km thickness deforms by frictional sliding, modeled using Byerlee's law. The crust overlies a dry mantle lithosphere, which extends to 80 km depth and is modeled using rheological properties for dry olivine. The zone between approximately 10 and 38 km (the dotted line) is characterized by semi-brittle behavior. Below 80 km, a wet olivine rheology is used to model the asthenosphere, following Hirth and Kohlstedt (1996). The inset shows the contrast in strength between stiff dry lithosphere and convecting wet asthenosphere.

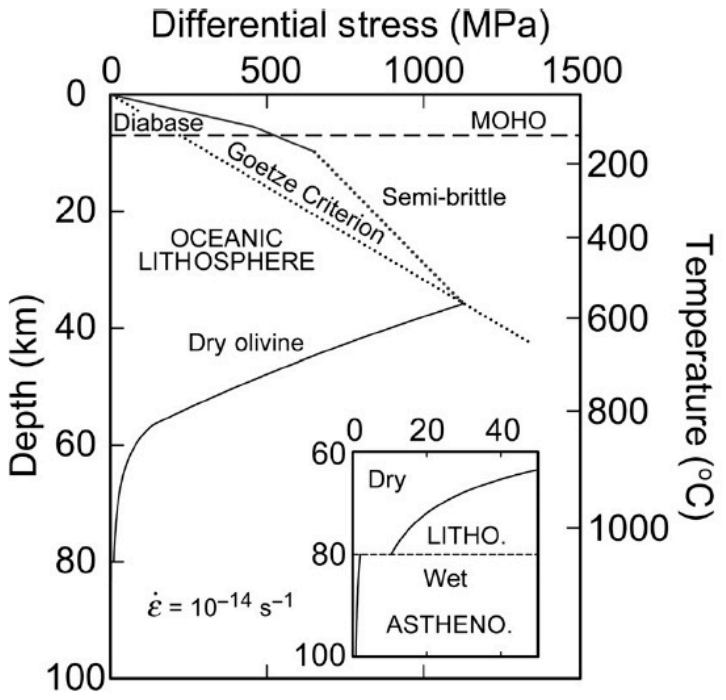

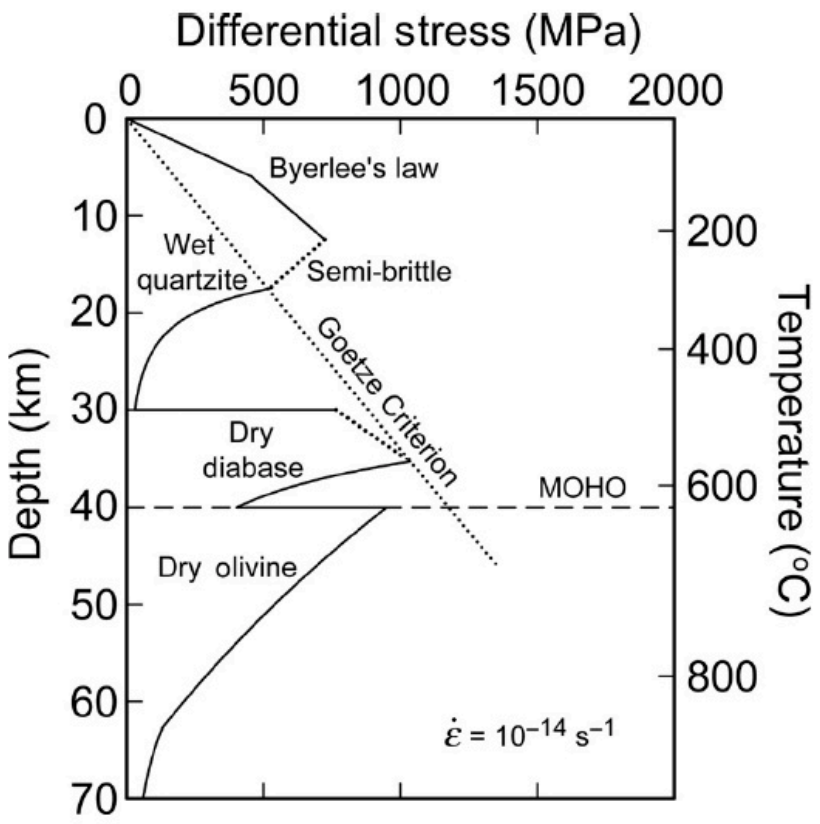

Figure 9.6. Strength envelope plot showing rock strength as a function of depth in the Earth for a model continental lithosphere deforming at a strain rate of 10^{-14} s^{-1}. A continental geotherm from Chapman (1986) for a surface heat flow of 60 mW/m was assumed. An upper crust of wet quartzite deforms at shallow depths by frictional sliding, and greater depths by dislocation creep. A dry lower crust (at amphibolite–granulite metamorphic conditions) composed of gabbroic composition rocks is modeled using rheological properties for dry diabase. Deformation in the olivine-rich mantle lithosphere is modeled by dislocation glide of dry olivine to about 60 km depth and by dislocation creep of dry olivine at greater depths. Semi-brittle regions exist in both the upper crust and lower crust; these regions are bounded below by the Goetze criterion.

Oceanic Lithosphere

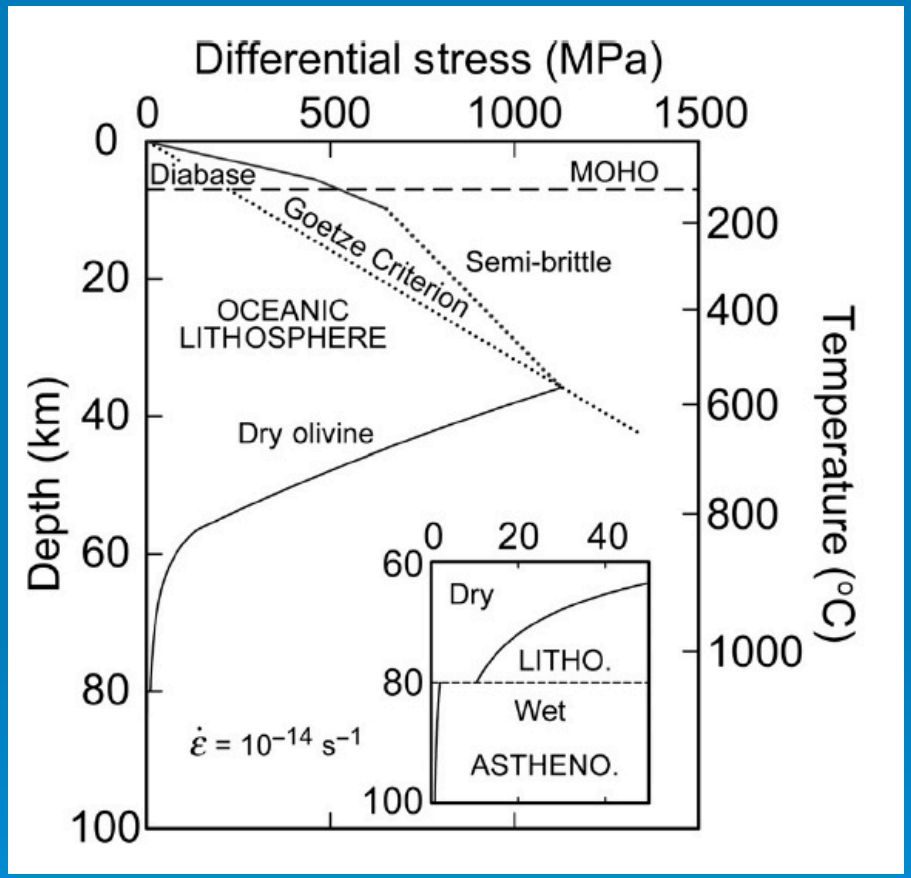

Continental Lithosphere

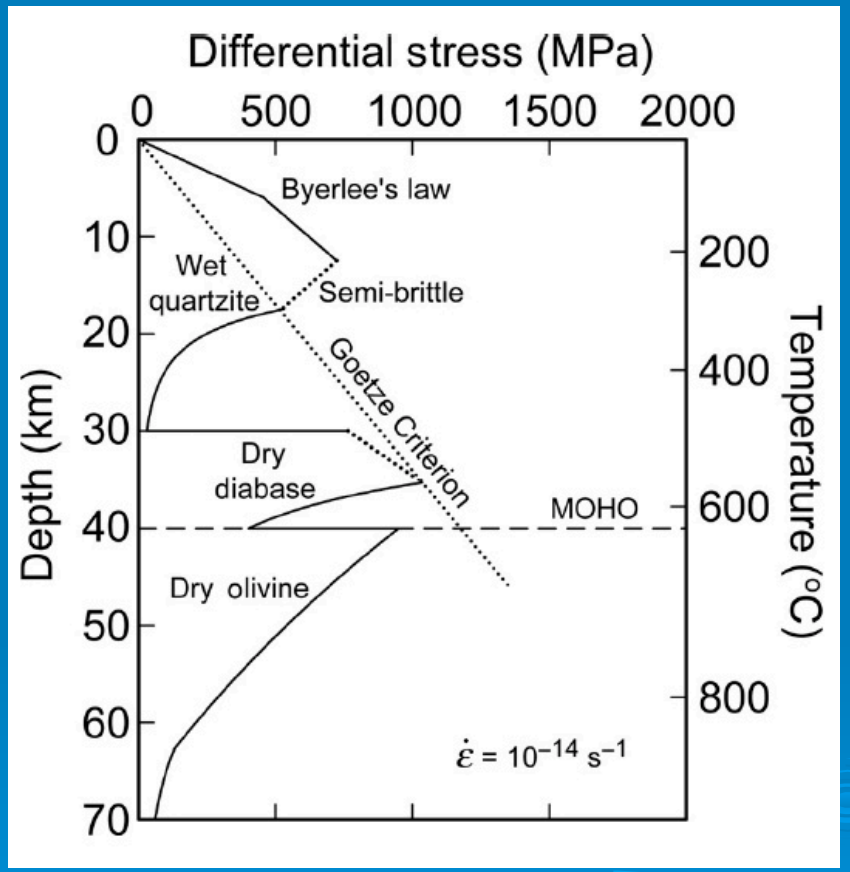

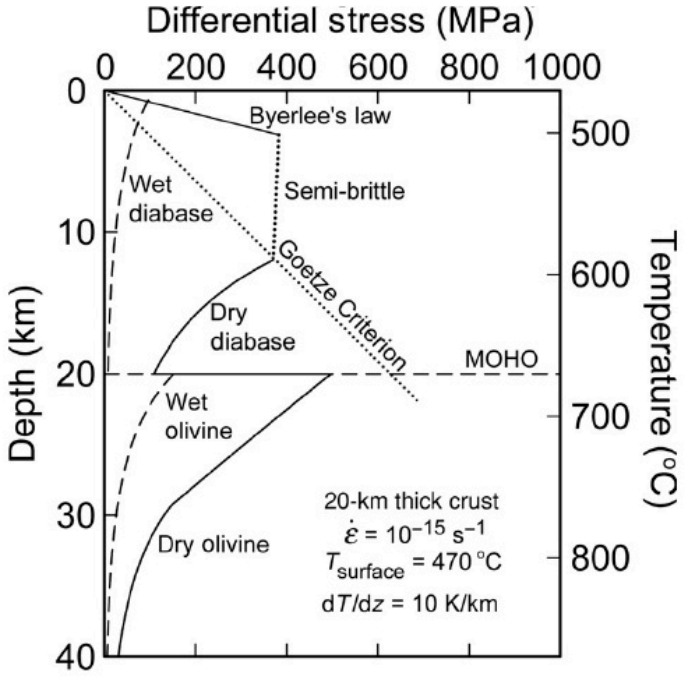

Figure 9.7. Strength envelope plotting rock strength as a function of depth in Venus for a lithosphere deforming at a strain rate of $10^{-15}\ s^{-1}$. We assumed a surface temperature of 470 °C, a thermal gradient of 10 K/km, and a crustal thickness of 20 km, conditions believed to be appropriate for Venus. A dry crust of basaltic composition was modeled at shallow depths by a frictional sliding law (Byerlee's law) and at greater depths by rheological properties for dry diabase deforming by dislocation creep. A significant region of semi-brittle behavior controls deformation over much of the crust. Rheology properties for wet diabase, included for comparison, predict an unrealistically weak crust for Venus. The mantle lithosphere, which is presumed to be strongly depleted in water, is modeled using rheological properties for dislocation glide (to about 30 km depth) and dislocation creep (at greater depths) for olivine under dry conditions. Due to long-term water loss from the mantle, no wet asthenosphere is expected on Venus.

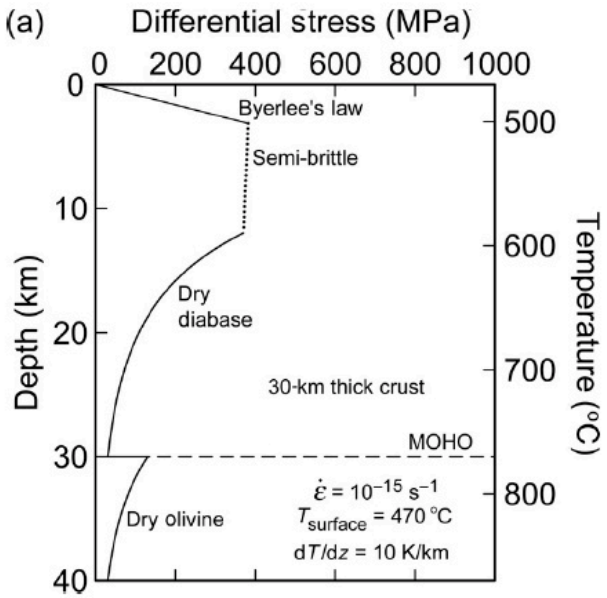

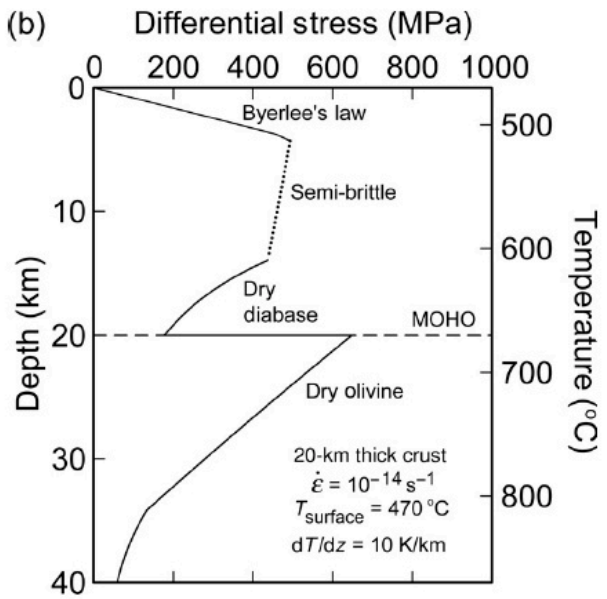

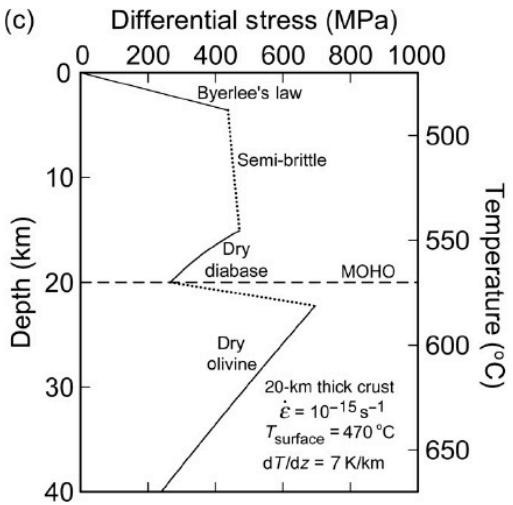

Figure 9.8. Strength envelope plotting rock strength as a function of depth in Venus to illustrate the effects of variation in (a) crustal thickness, (b) strain rate, and (c) thermal gradient by comparison to the boundary conditions used in Figure 9.7. Increasing crustal thickness resulted in a somewhat weaker lithosphere overall, while both increased strain rate and decreased thermal gradient strengthened the lithosphere. However, despite these changes in overall strength, all models still predict a strong lithosphere and strong mechanical coupling between crustal and mantle regions.

A Historical Perspective for Tectonics Research in Past Decades

Before 1960: The dark age.

1960s: Invention of plate tectonics.

1970s: Testing and Confirming Plate Tectonics in oceanic domains and ancient orogenic belts.

1980s-pesent: Realization and investigation of how and why active continental deformation differs so significantly from oceanic deformation.

Major testing grounds: Asia and western North America.

Plate tectonics: Rigid plates moving in the outer layer of the Earth

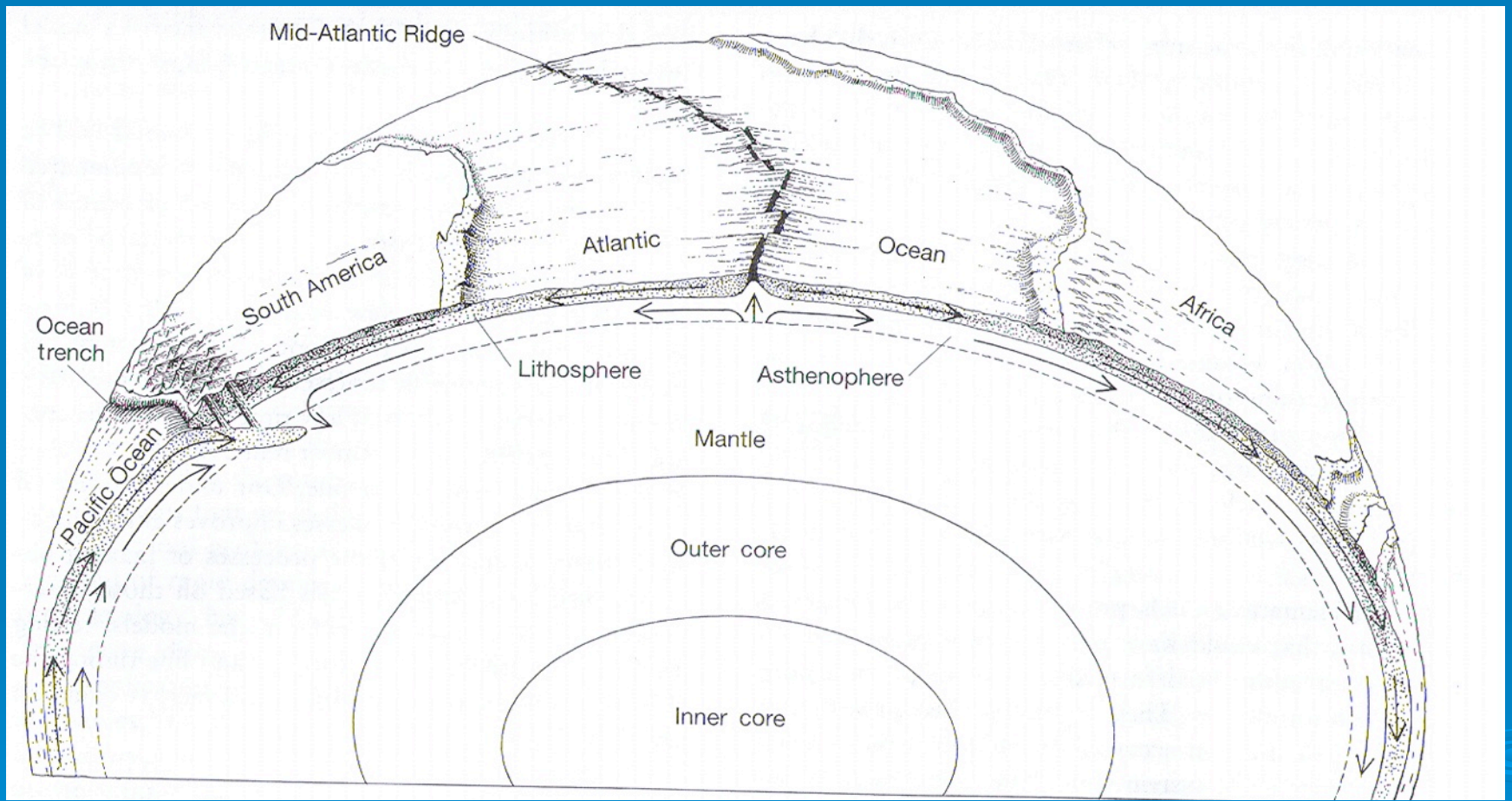

It works best for the oceanic plates, but quite poorly in parts of continents!

Sharp Plate Boundaries in the Oceanic Domain

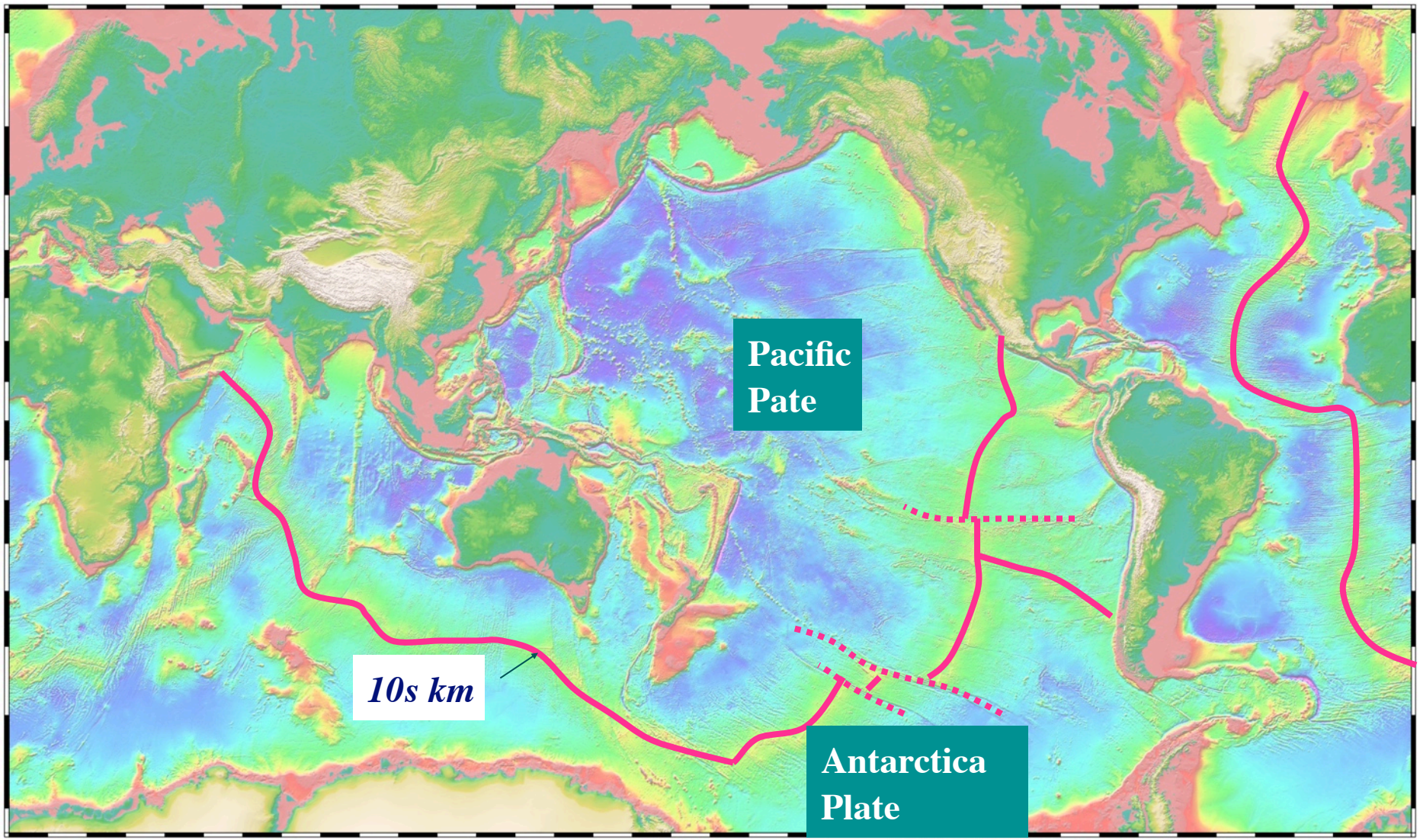

Very Wide Plate Boundary Zones in Continental Domain

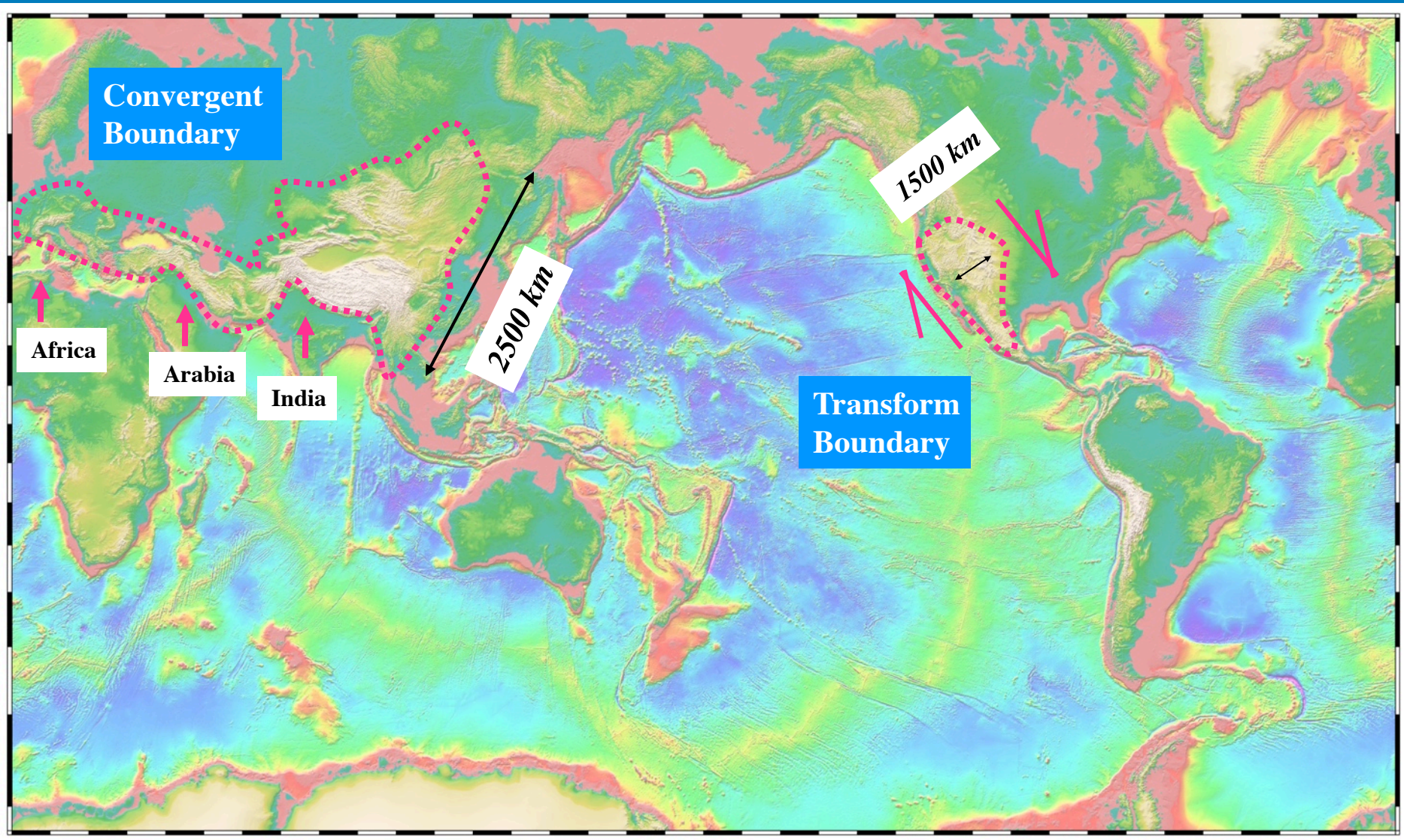

Seismicity in Tibet

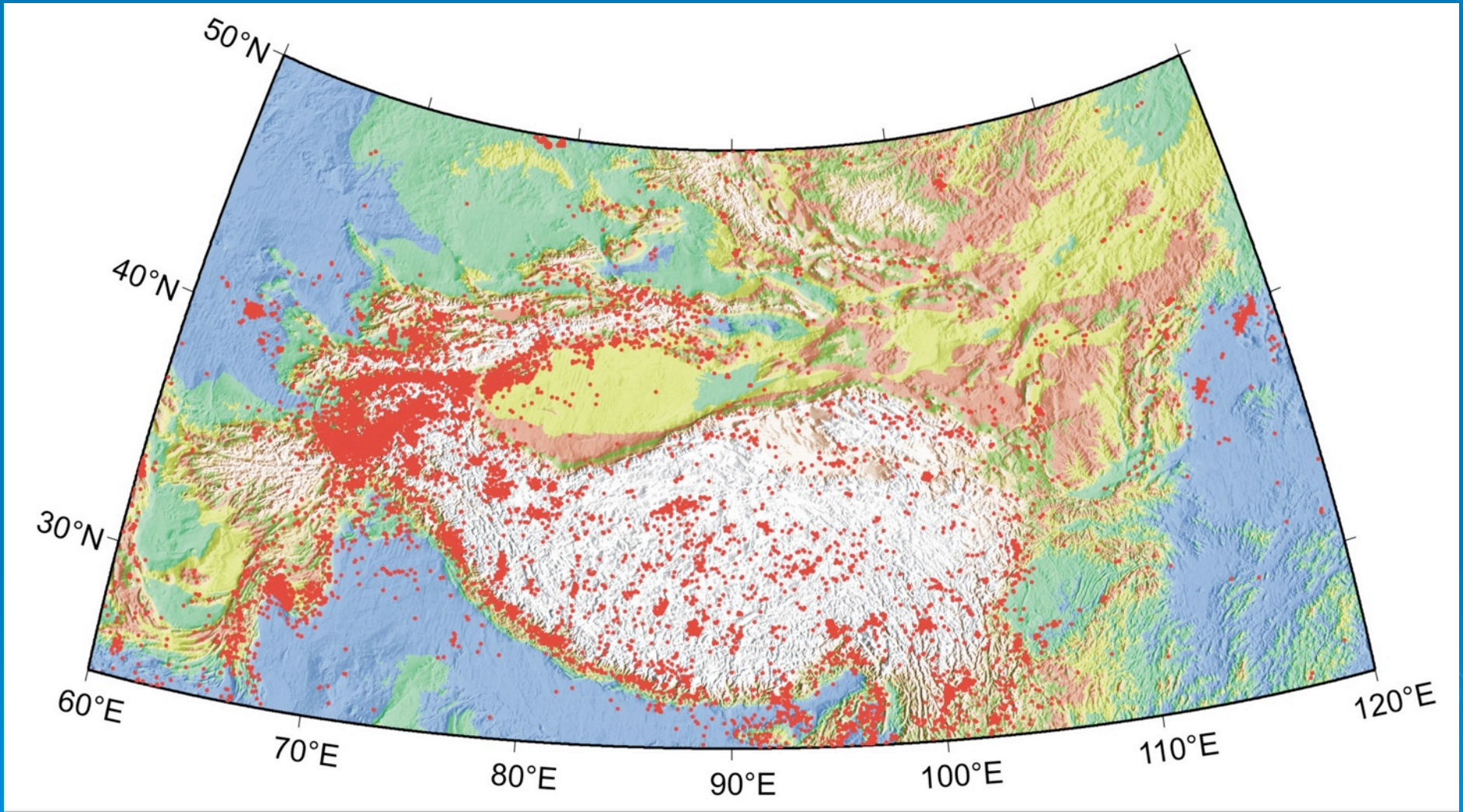

Models of Continental Deformation

Micro-plate model

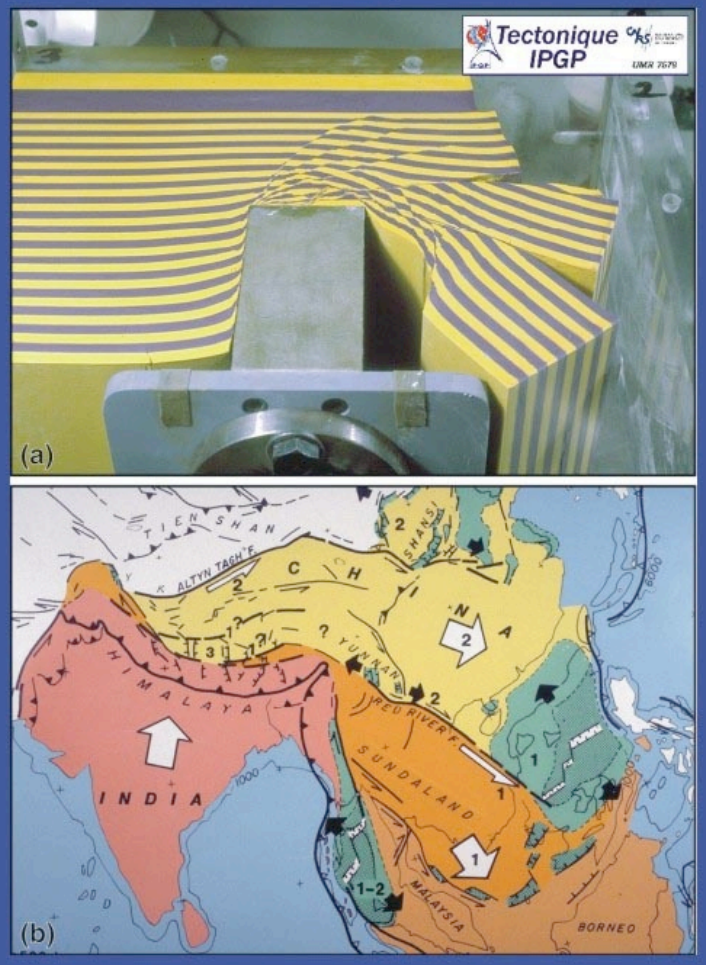

Tectonic Extrusion

A. (Peltzer and Tapponnier, 1988; Tapponnier et al., 1982).
B. Two stage extrusion model (Tapponnier et al., 1986).

Thin Viscous Sheet Model

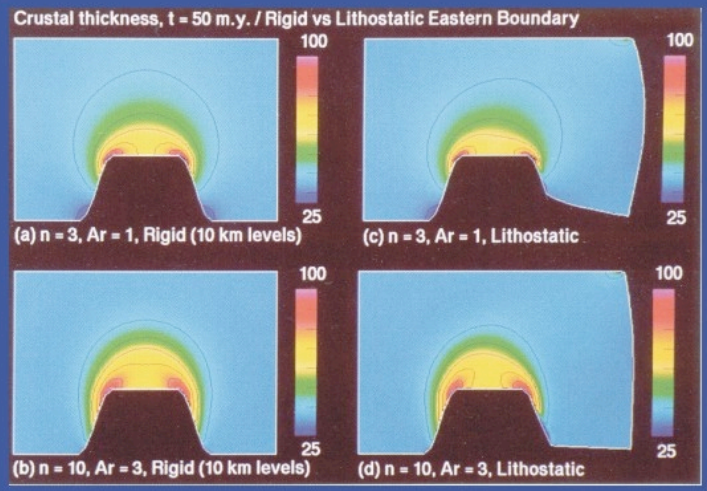

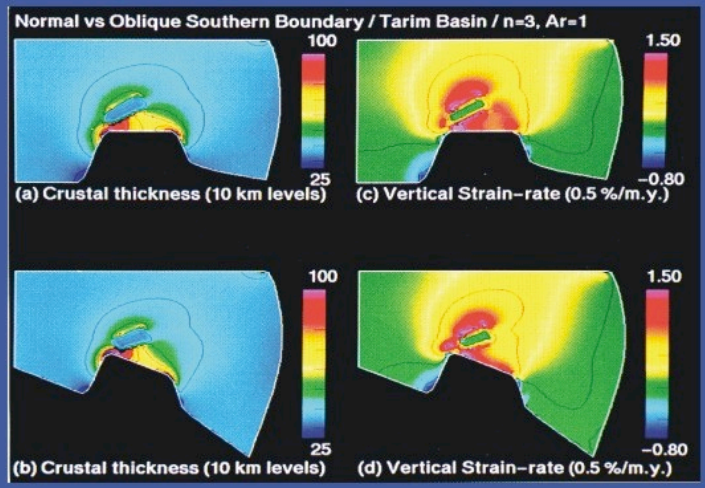

Houseman and England, 1996

Predictions of the two models:

Micro-plate Model (also known as the "extrusion model"): ***A few large faults with fast slip rates bounding little deformed continental blocks. – Kinematic Problem***

Thin Viscous Sheet Model (also known as the "distributed deformation model"): ***All faults were created equal, each having small displacement and slow slip rates. Overall deformation field can be approximated by viscous flow. – Dynamic Problem and Need to Know Rheology***

We leave this debate for later discussion and examine first some of the fundamental problems in rock mechanics.

Conjugate faults created by Coulomb fracture experiments

Two shear fractures formed at 30^0 angle from the maximum compressive stress direction

From Andreas Kronenberg's website at Univ. Texas A&M
http://geoweb.tamu.edu/Faculty/Kronenberg/K615.html


11/22/2010 01:56


11/22/2010 01:56

V-shaped Conjugate Strike-slip faults in Asia

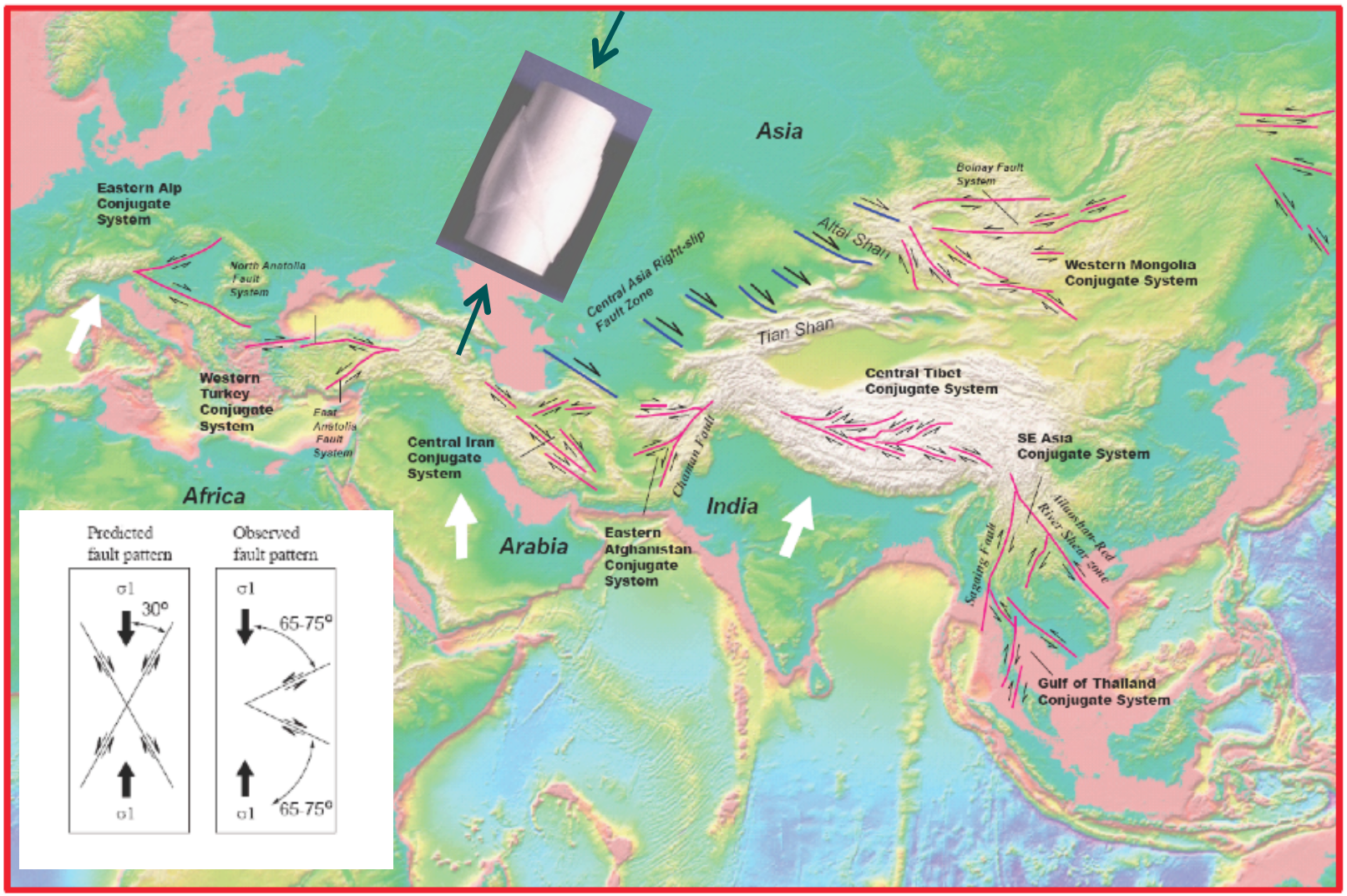

Tharsis Rise

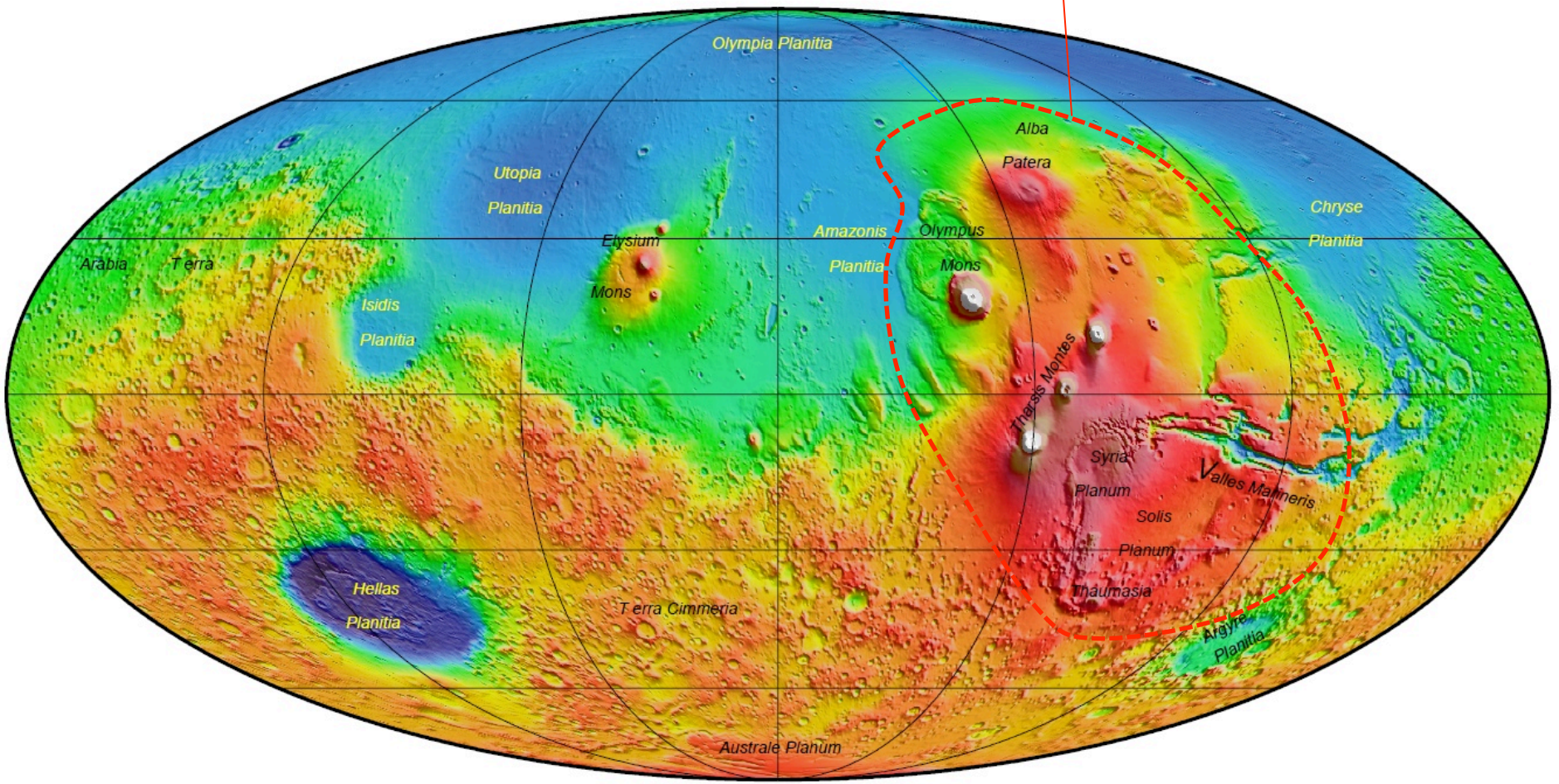

Conjugate system: Right-slip faulting along Clarita Fossae (CF) and Left-slip faulting along Valles Marineris (VM)

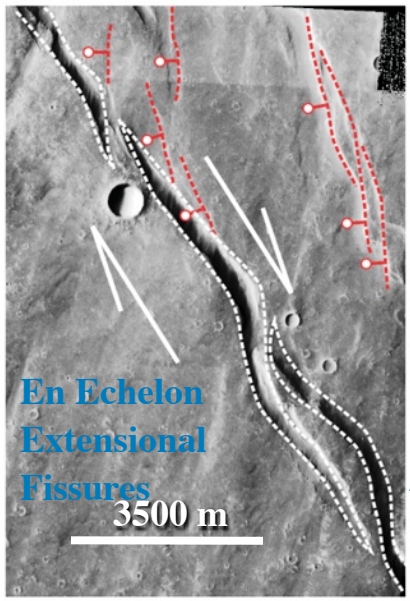

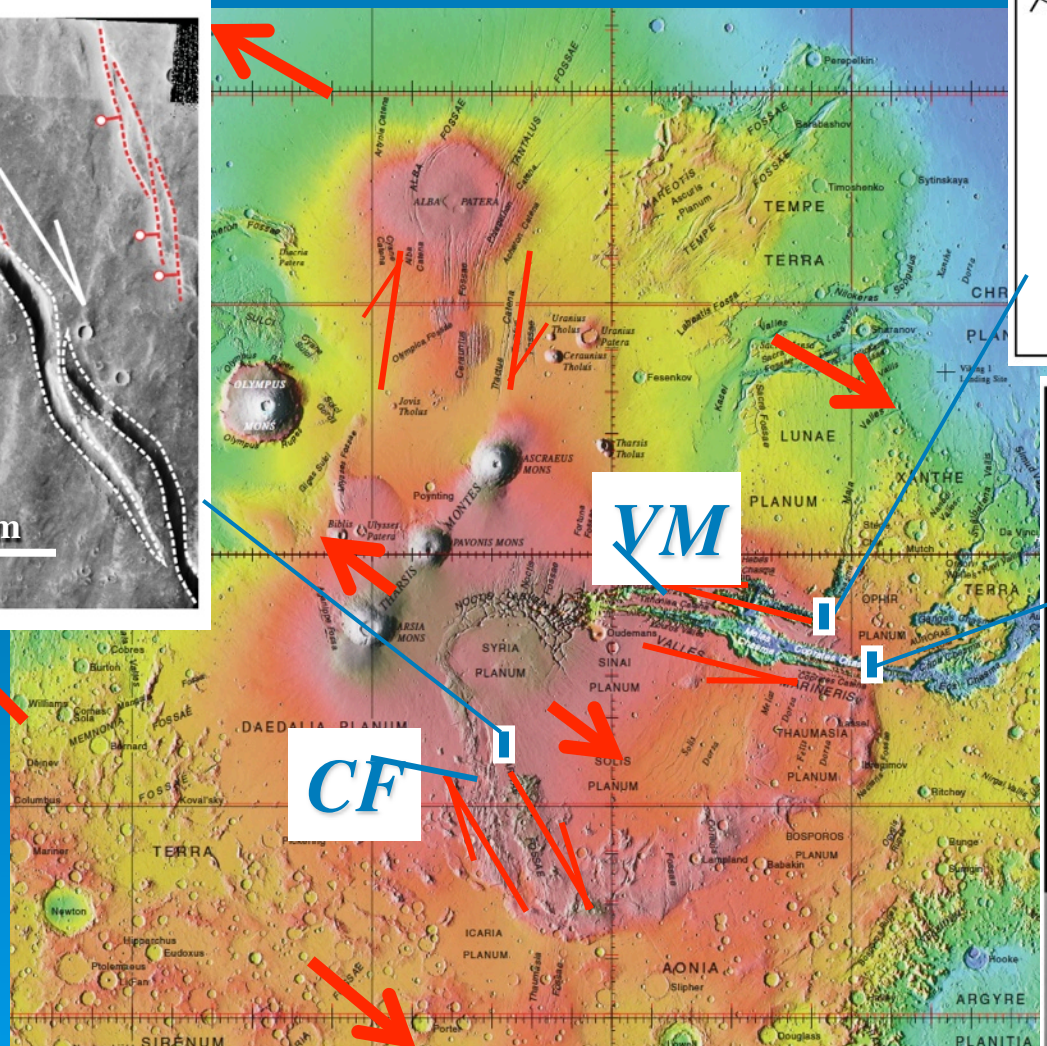

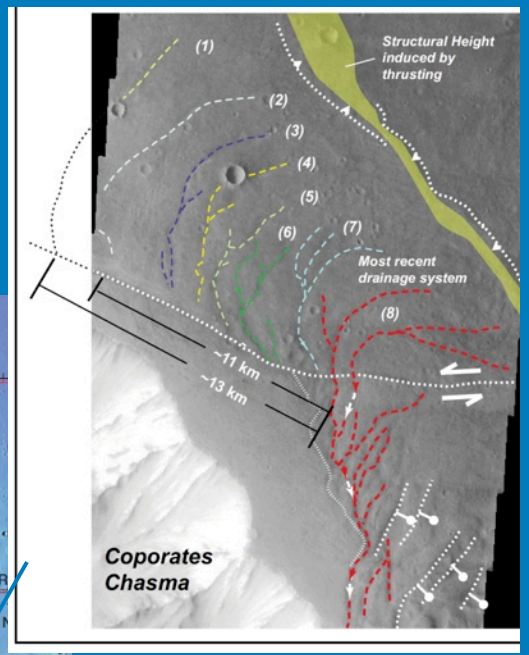

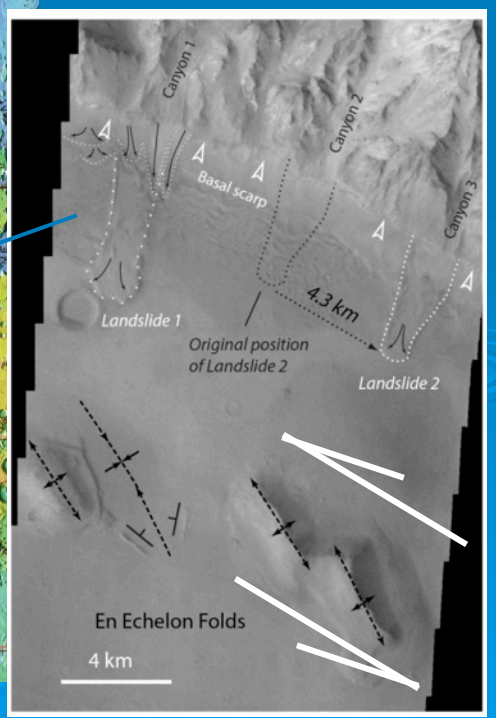

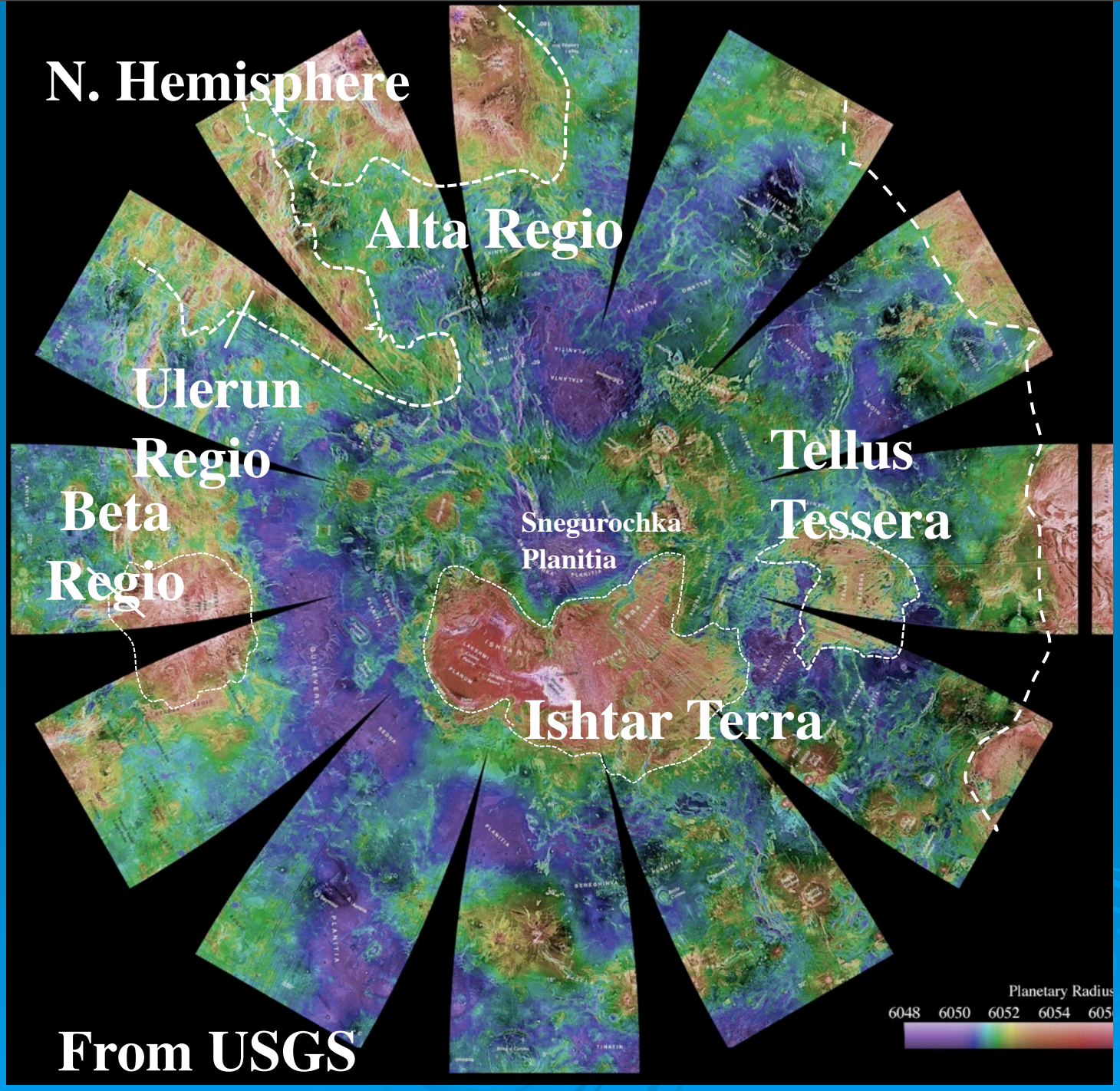
N. Hemisphere
Alta Regio
Ulerun Regio
Beta Regio
Tellus Tessera
Snegurochka Planitia
Ishtar Terra
Planetary Radius
6048 6050 6052 6054
From USGS

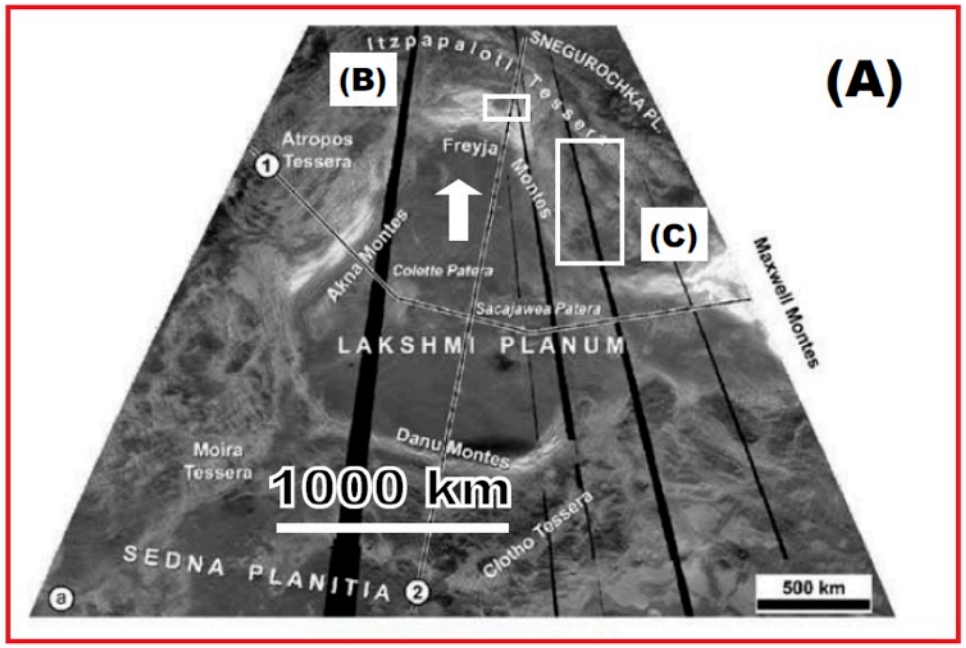

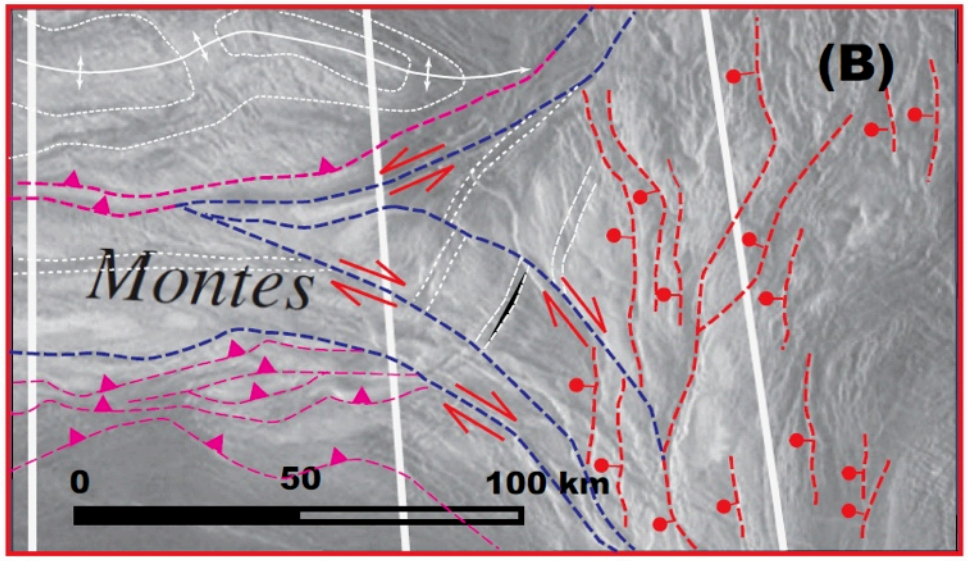

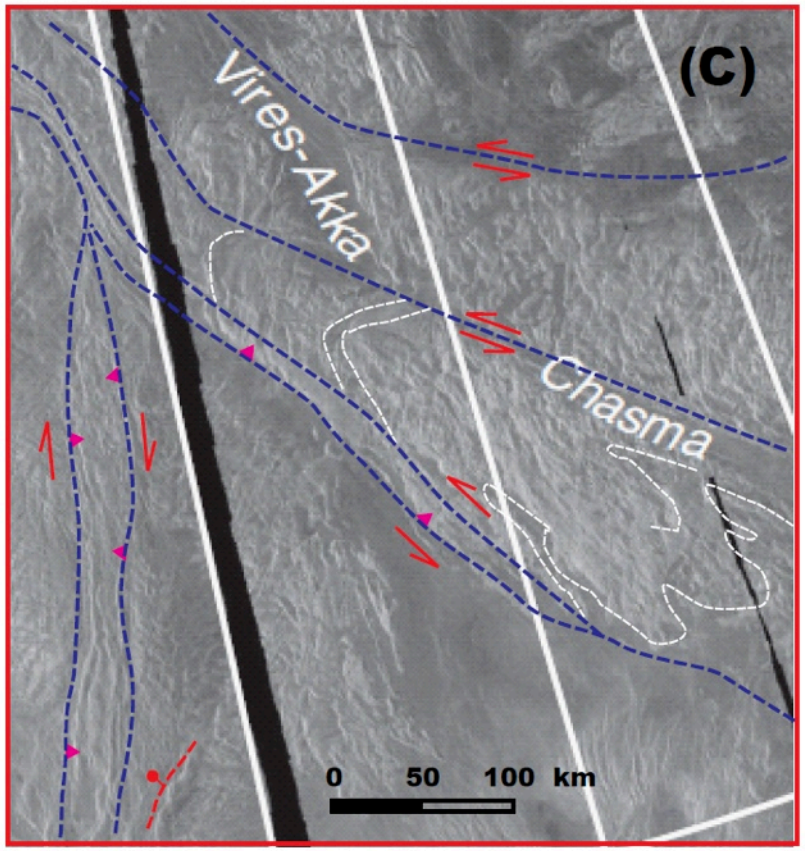

Figure 3. (A) Location of the Lakshmi in Ishta Terra in northern hemisphere of Venus, from Ivanov and Head (2008). Northward motion of Lakshmi planum created the Freyia Montes in front of the indenter and V-shaped conjugate strike-slip systems to the north (B) and and the east (C).

V-shaped Conjugate Strike-slip faults in Asia

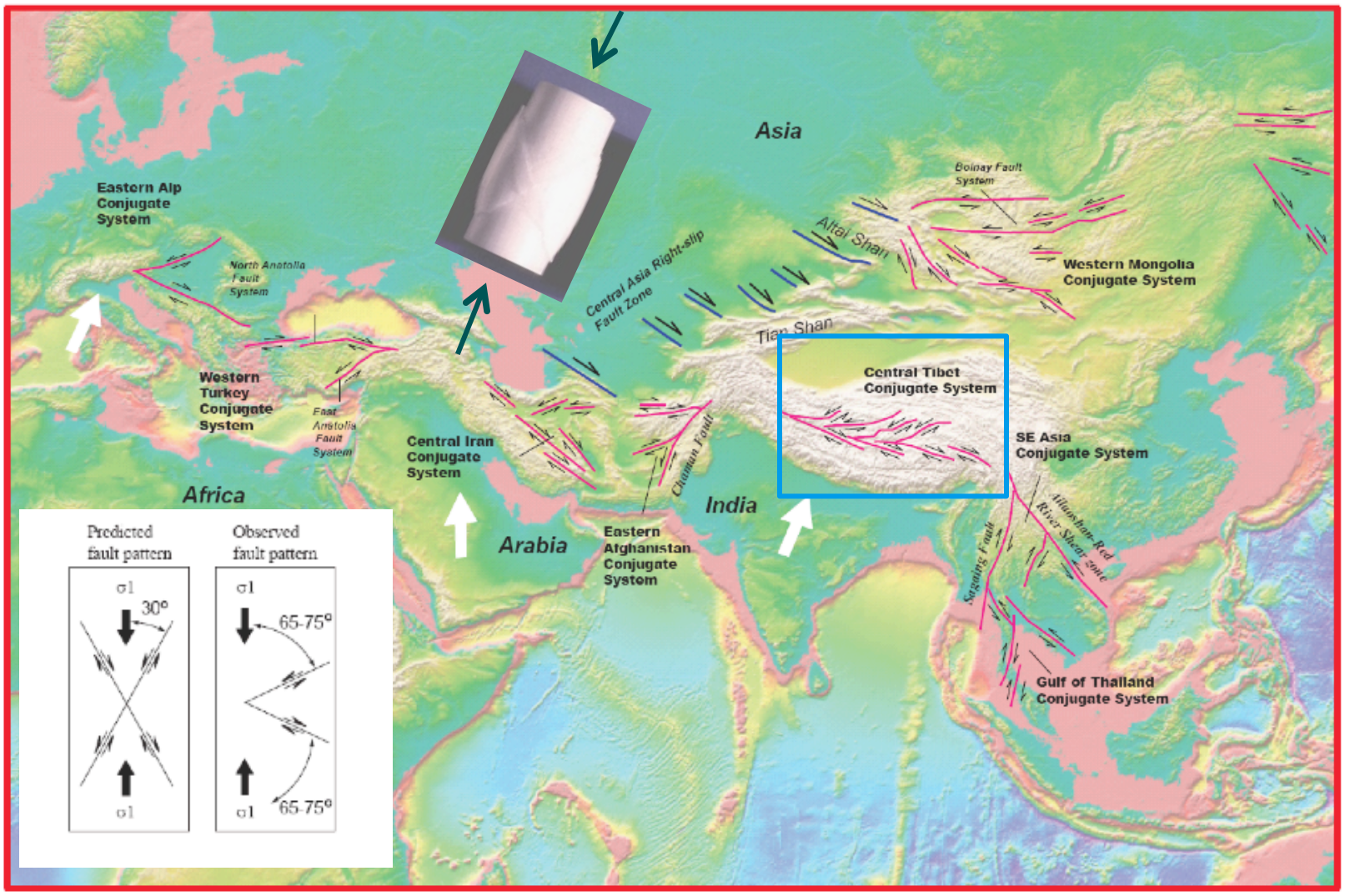

Active Central Tibet Conjugate Fault Zone

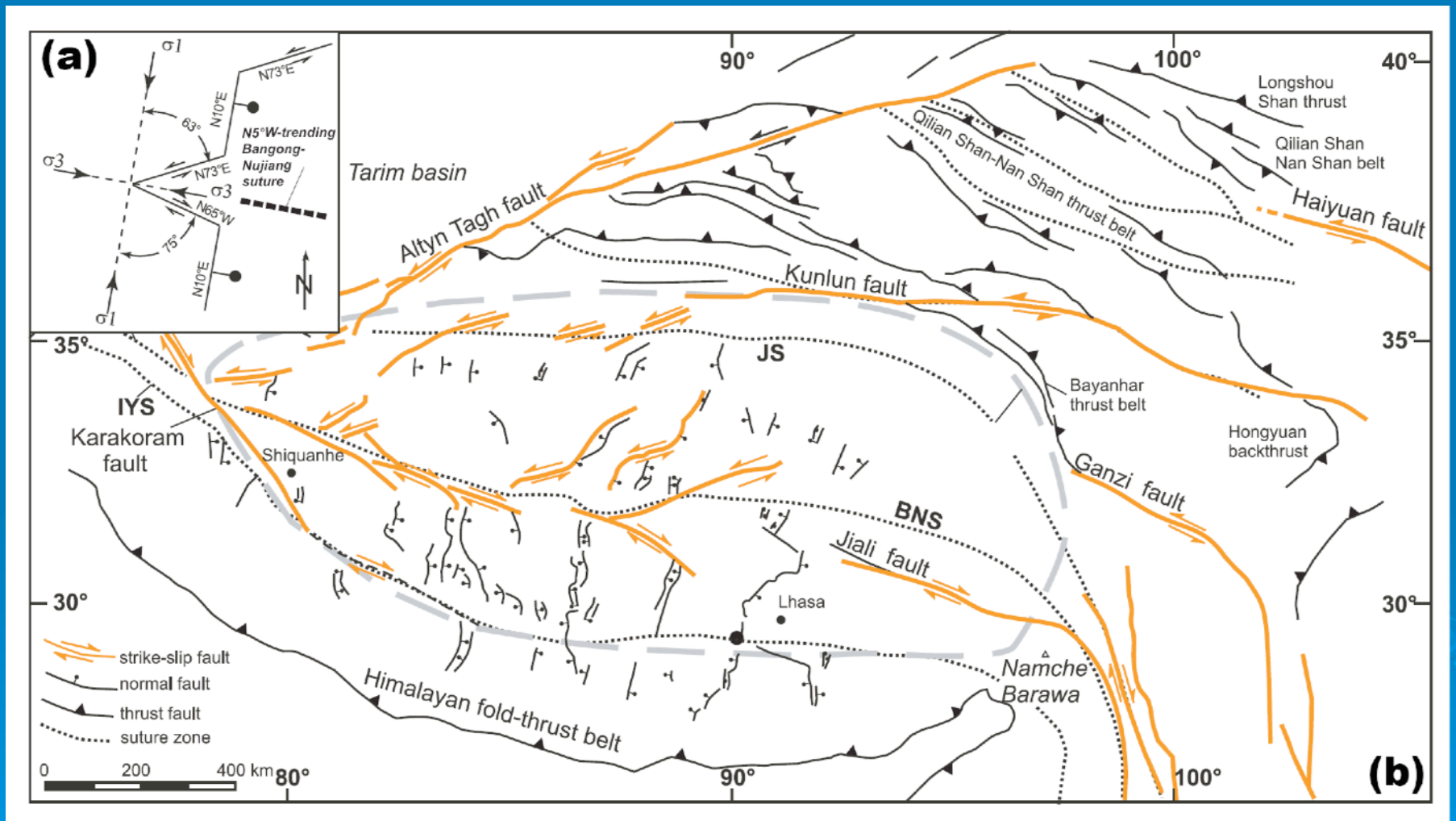

After Taylor et al. (2003, Tectonics)

Tibetan Conjugate Faults:

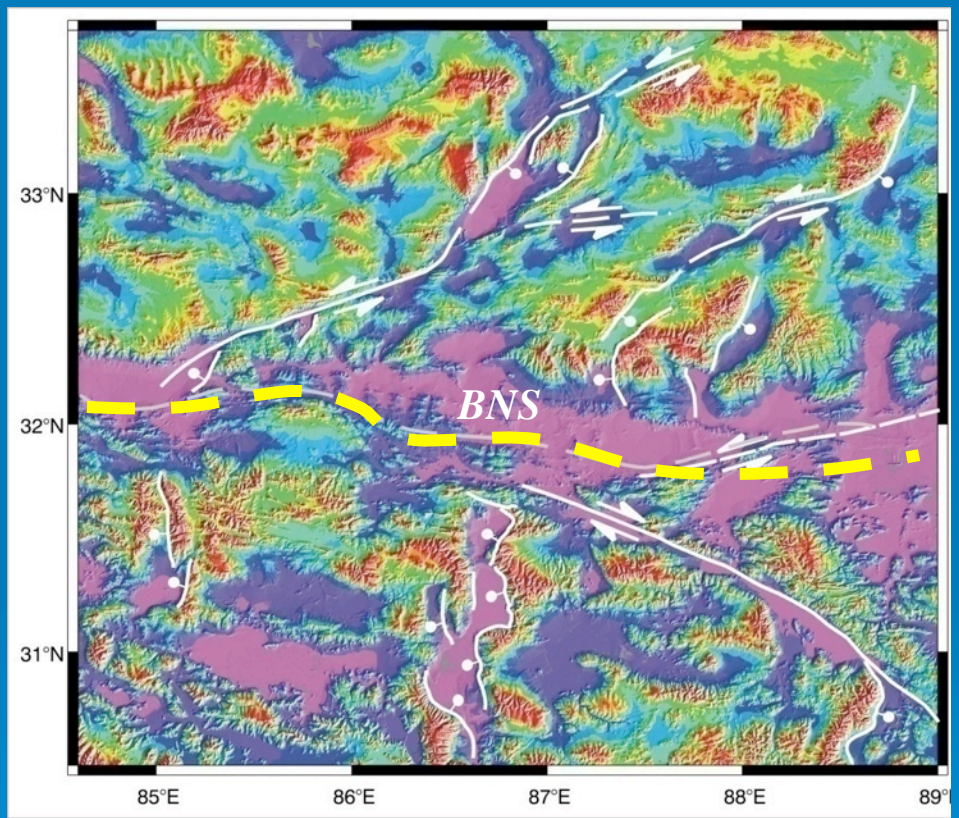

After Taylor et al. (2003, Tectonics)

1. Initiated at ~ 14-8 Ma, with 8-12 km slip.

2. Major faults are spaced at ~100-150 km and currently active.

3. Bangong-Nujiang suture (BNS) divides the left-slip faults to the north and right-slip faults to the south

5. Little deformation in fault-bounded regions.

Without basal boundary conditions, all analogue models fail to predict Tibetan conjugate fault geometry

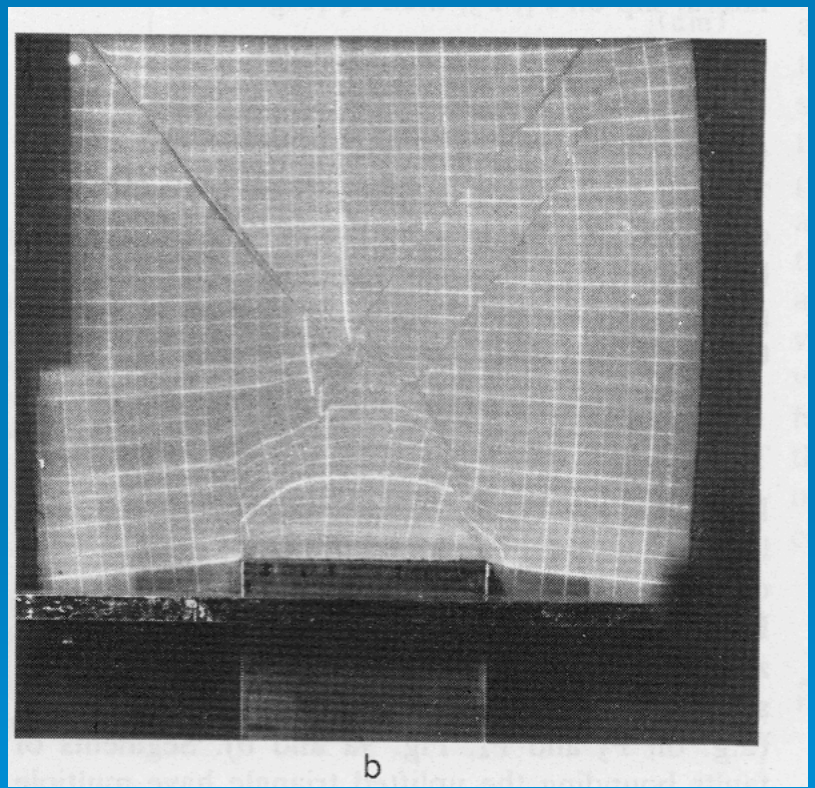

Peltzer (1988)

Observed fault orientations in central Tibet

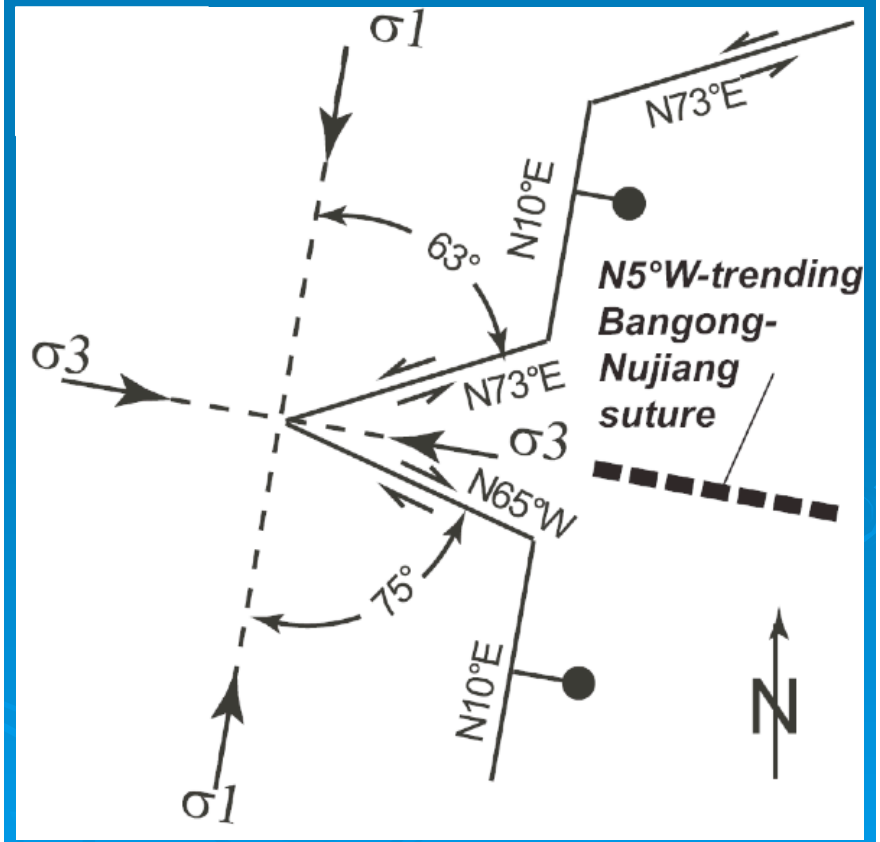

Fault Rotation by bookshelf faulting or Distributed Deformation

>100 km fault slip on individual faults

>40% north-south shortening after fault formation

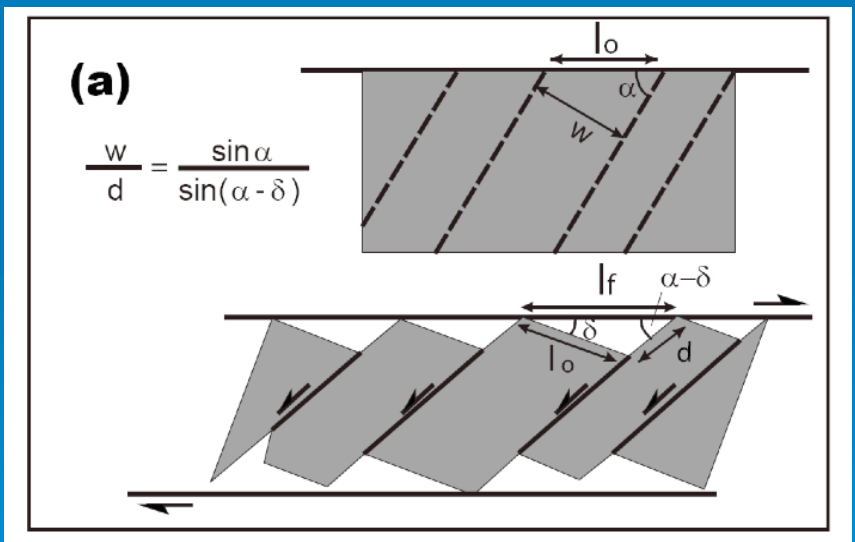

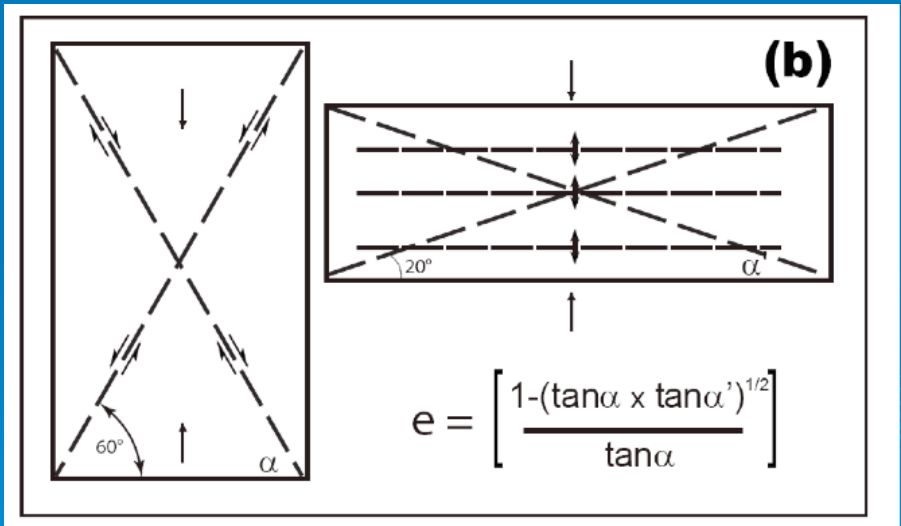

Bookshelf-style faulting (e.g., Freund, 1970)

Distributed deformation (Dewey et al., 1989)

Experimentally, there are two ways to make faults: "*pure shear*" (i.e., co-axial deformation) and "*simple shear*" (i.e., non-coaxial deformation) with different velocity boundary conditions.

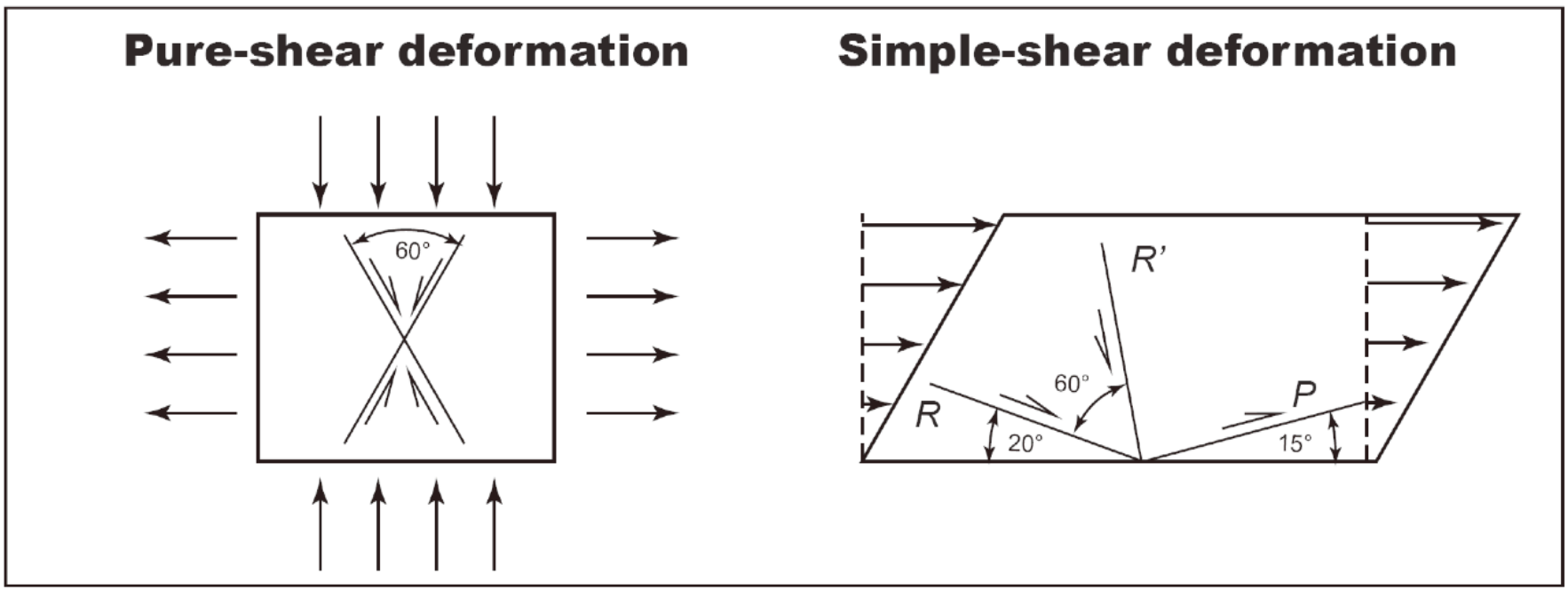

Coulomb shear fractures formed by coaxial (pure-shear) deformation

Initiation of shear fractures controlled by stress

Riedel shear fractures formed by non-coaxial (simple-shear) deformation

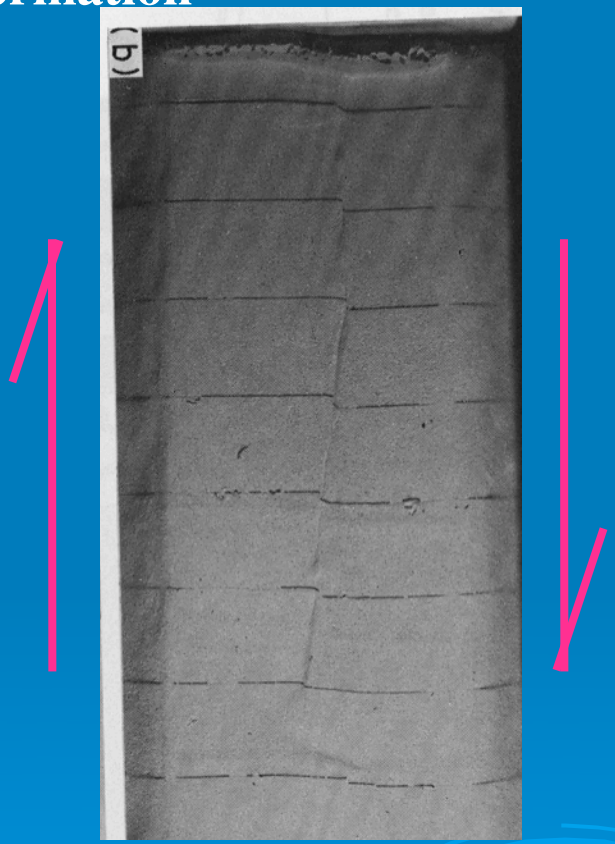

Initiation of shear fractures controlled by strain/strain rate (= flow!)

Central Tibet GPS Velocity Data

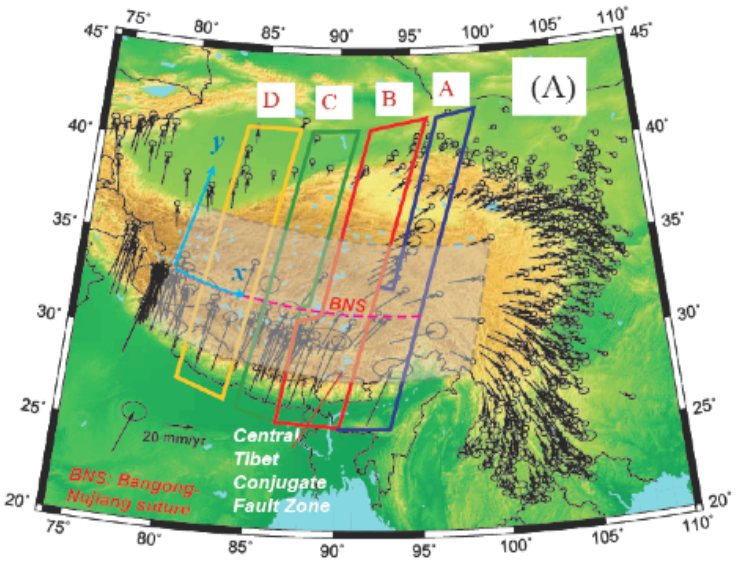

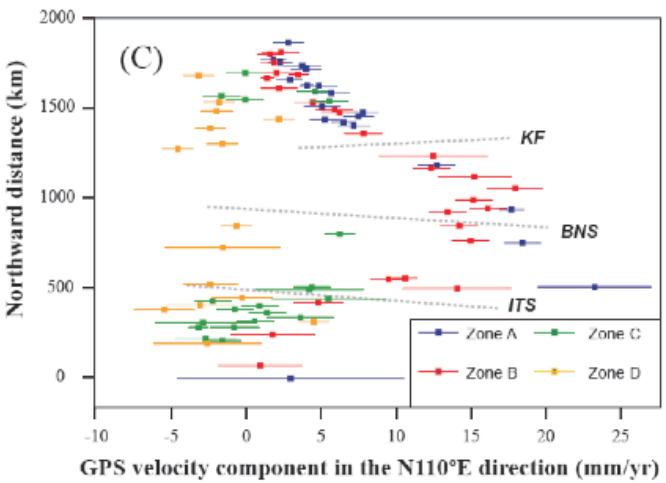

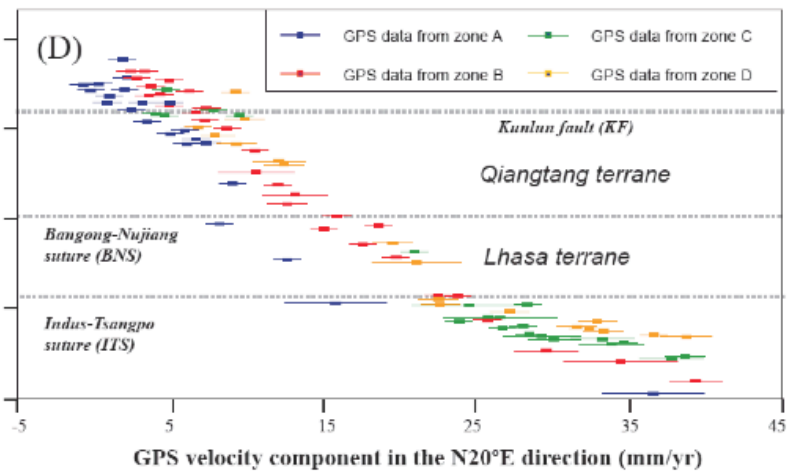

Analytical Approximation for GPS Velocity Field

$$u = \frac{S - U_0}{Lh^2} x(h^2 - 4y^2) + U_0$$

$$v = -\frac{V_0}{h} y$$

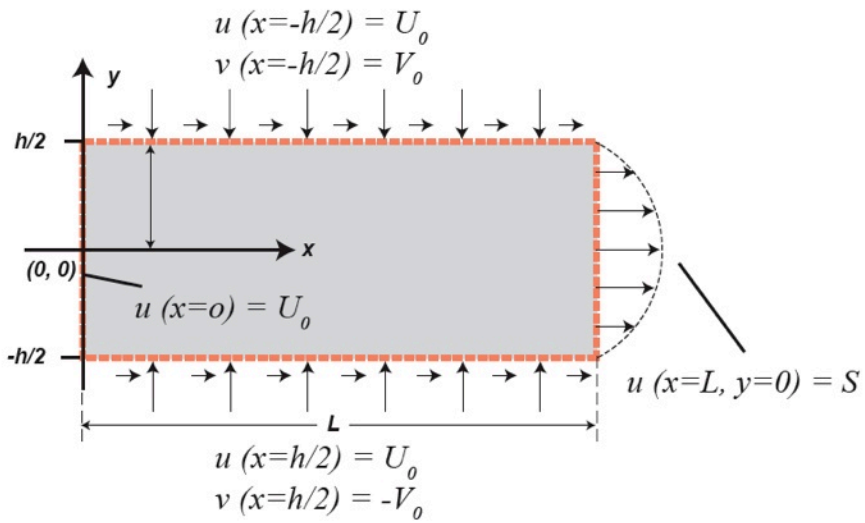

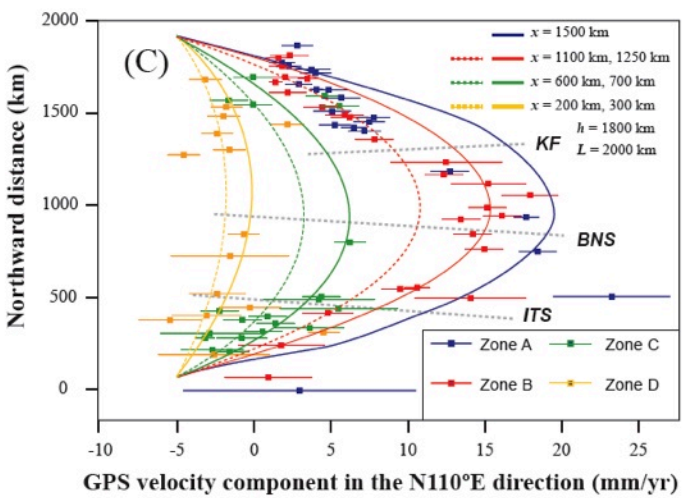

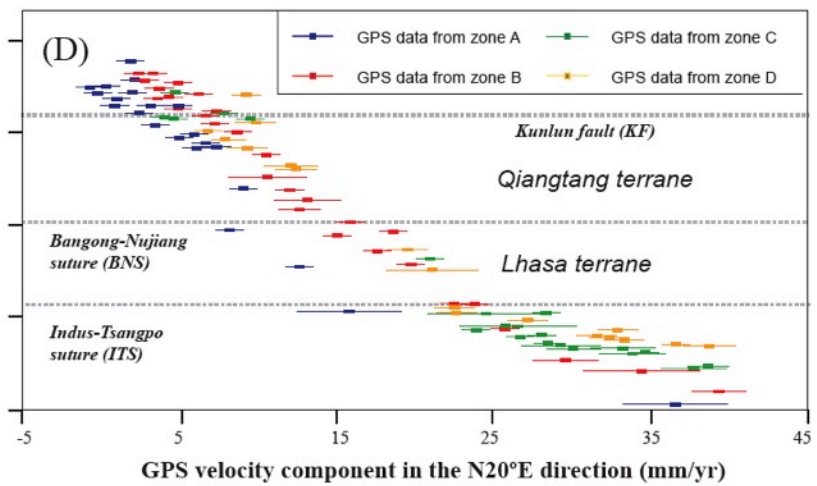

Strain-rate Field in Central Tibet

$$\dot{\varepsilon}_{xx} = \frac{S - U_0}{Lh^2}(h^2 - 4y^2)$$

$$\dot{\varepsilon}_{yy} = -\frac{V_0}{h}$$

$$\dot{\varepsilon}_{xy} = -8\frac{S - U_0}{Lh^2}xy$$

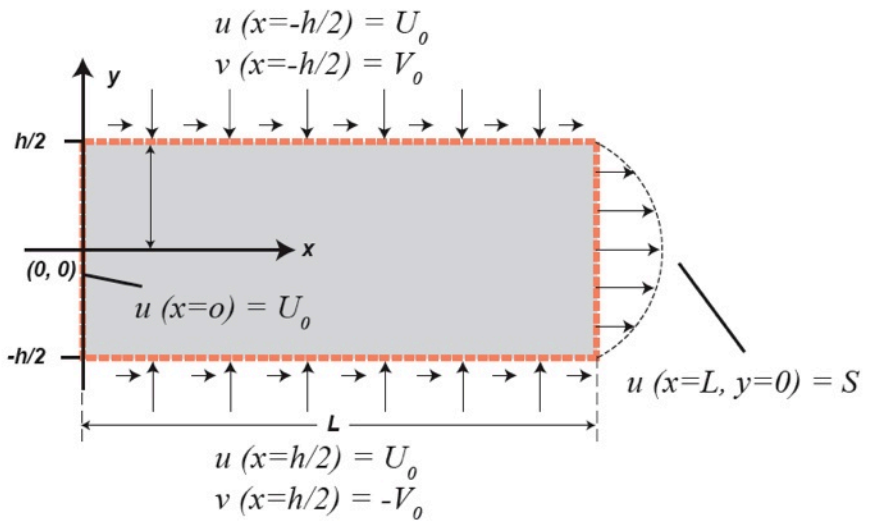

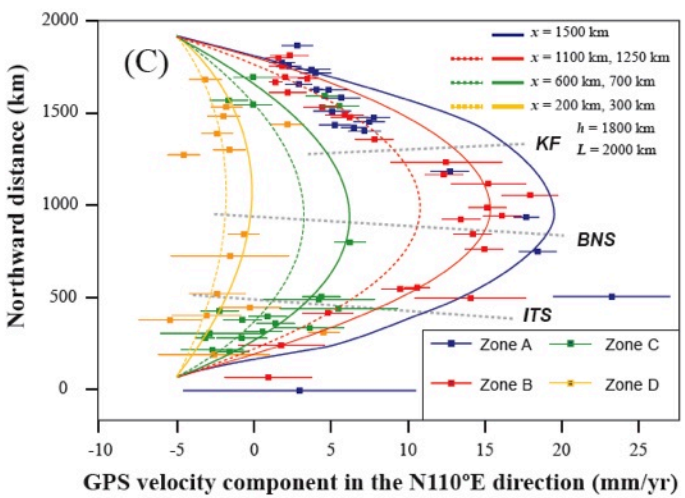

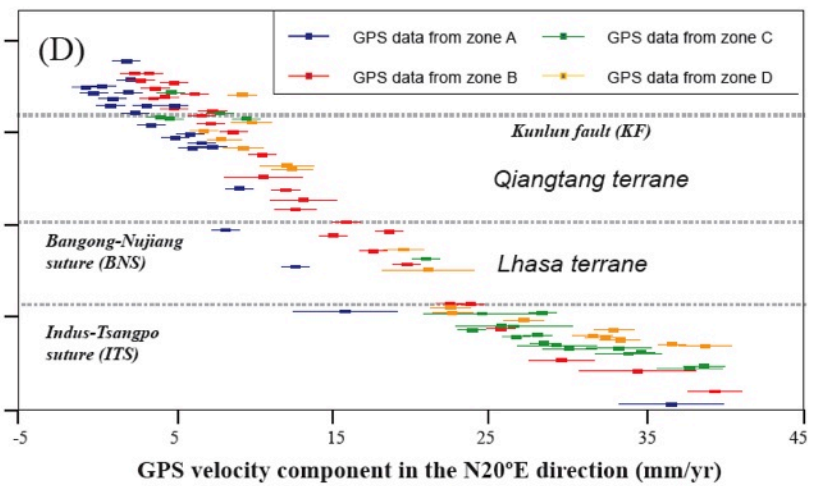

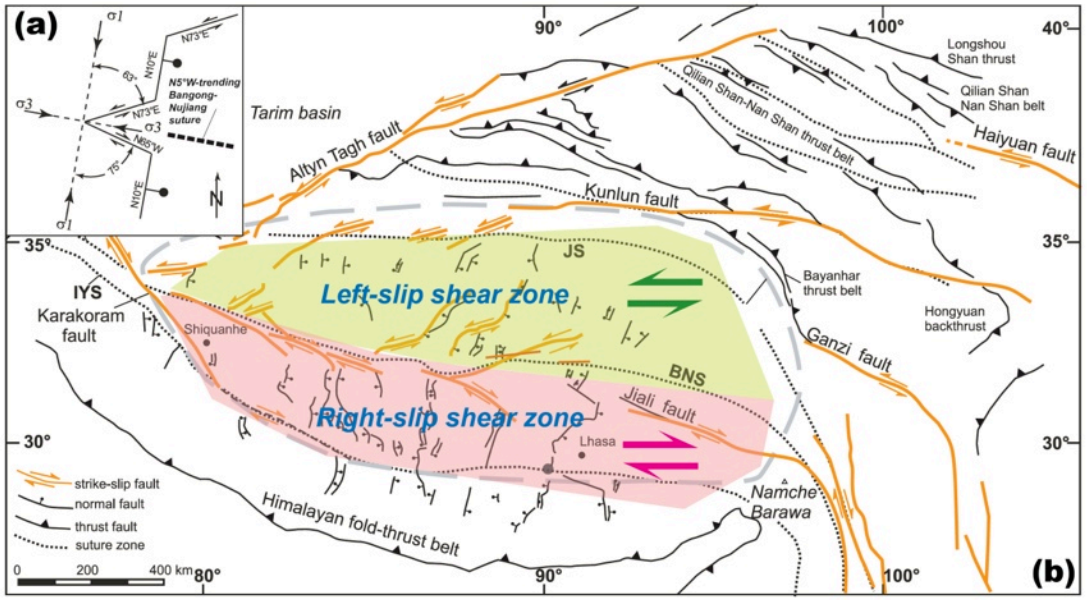

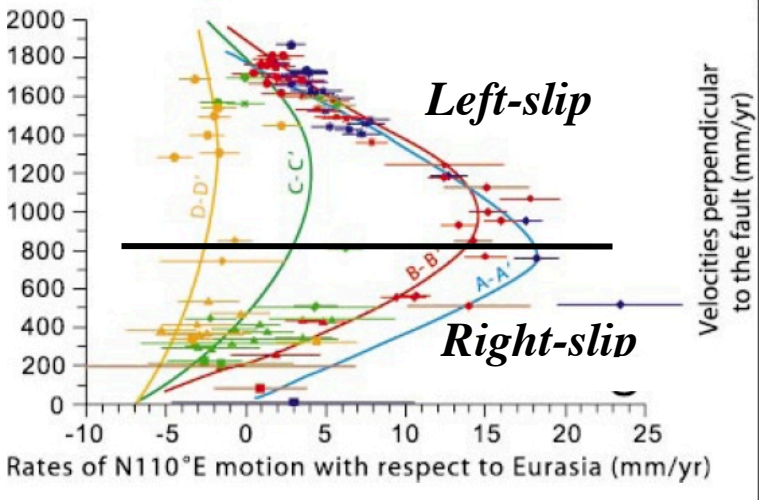

Paired simple-shear-zone model

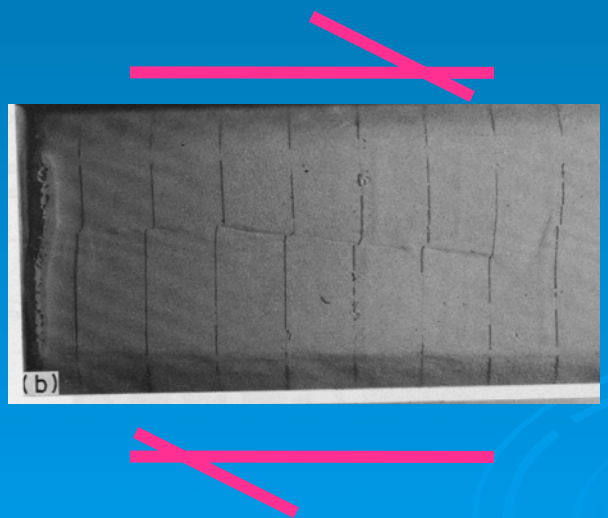

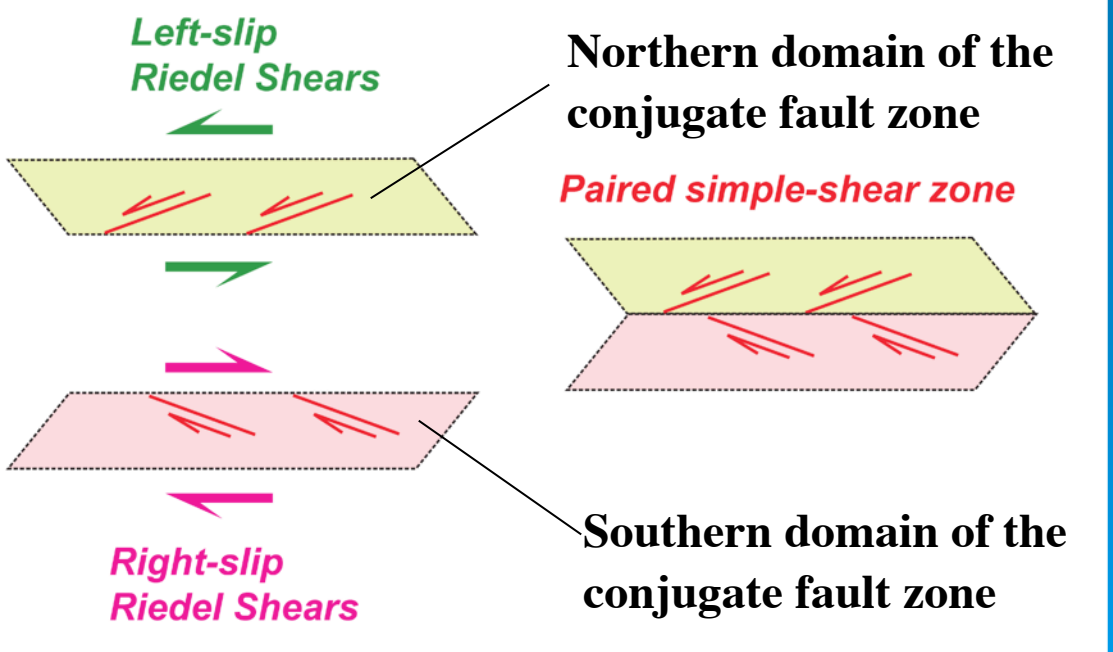

Predictions of the two models:

Micro-plate Model (also known as the "extrusion model"): ***A few large faults with fast slip rates bounding little deformed continental blocks.***

Thin Viscous Sheet Model (also known as the "distributed deformation model"): ***All faults were created equal, each having small displacement and slow slip rates. Overall deformation field can be approximated by viscous flow.***

We can now return to the debate: The development of V-shaped conjugate faults requires the presence of a paired simple shear zone or a modified Hagen-Poiseuille flow with two walls approaching each other.

V-shaped Conjugate Strike-slip faults in Asia

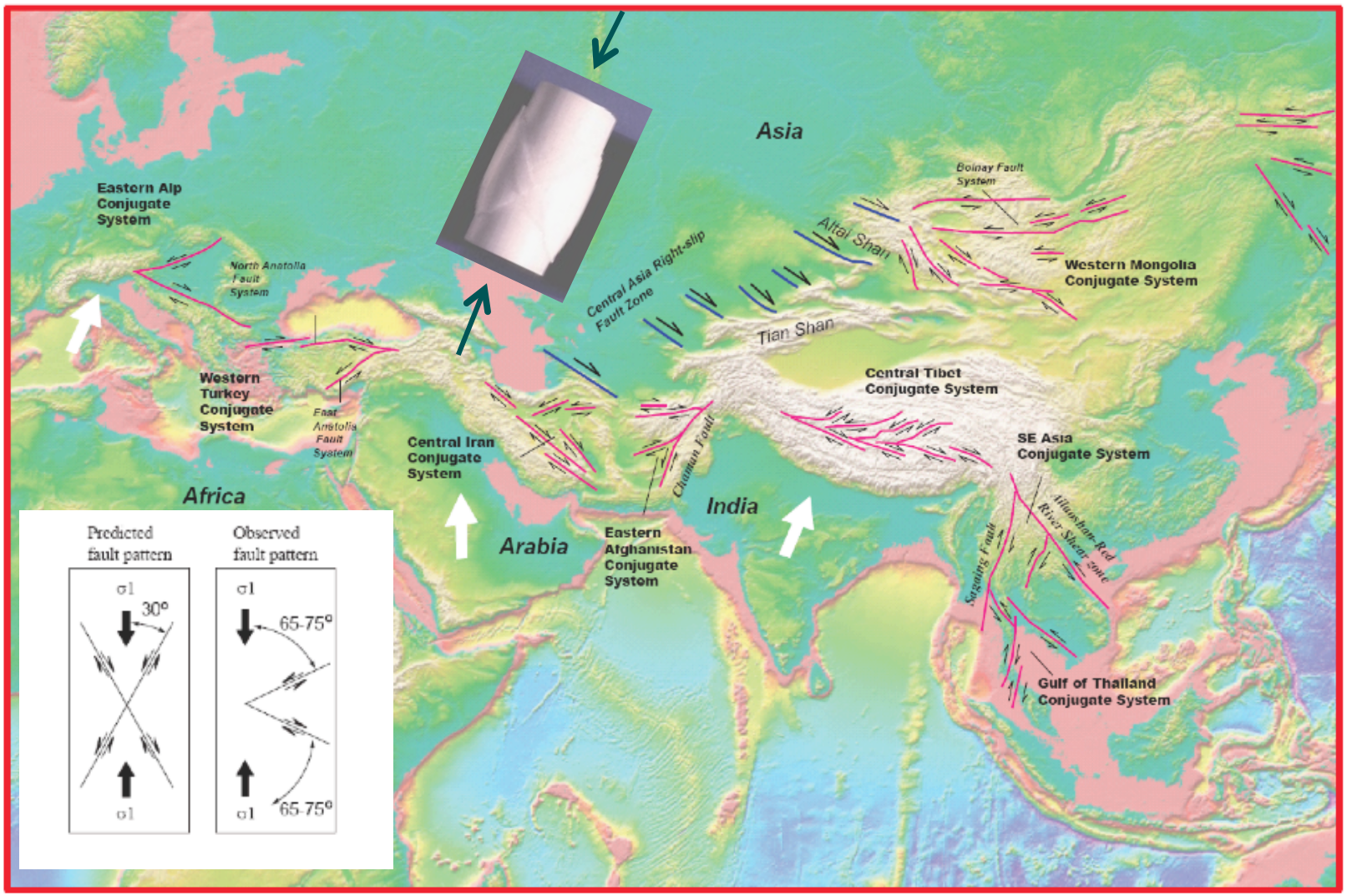

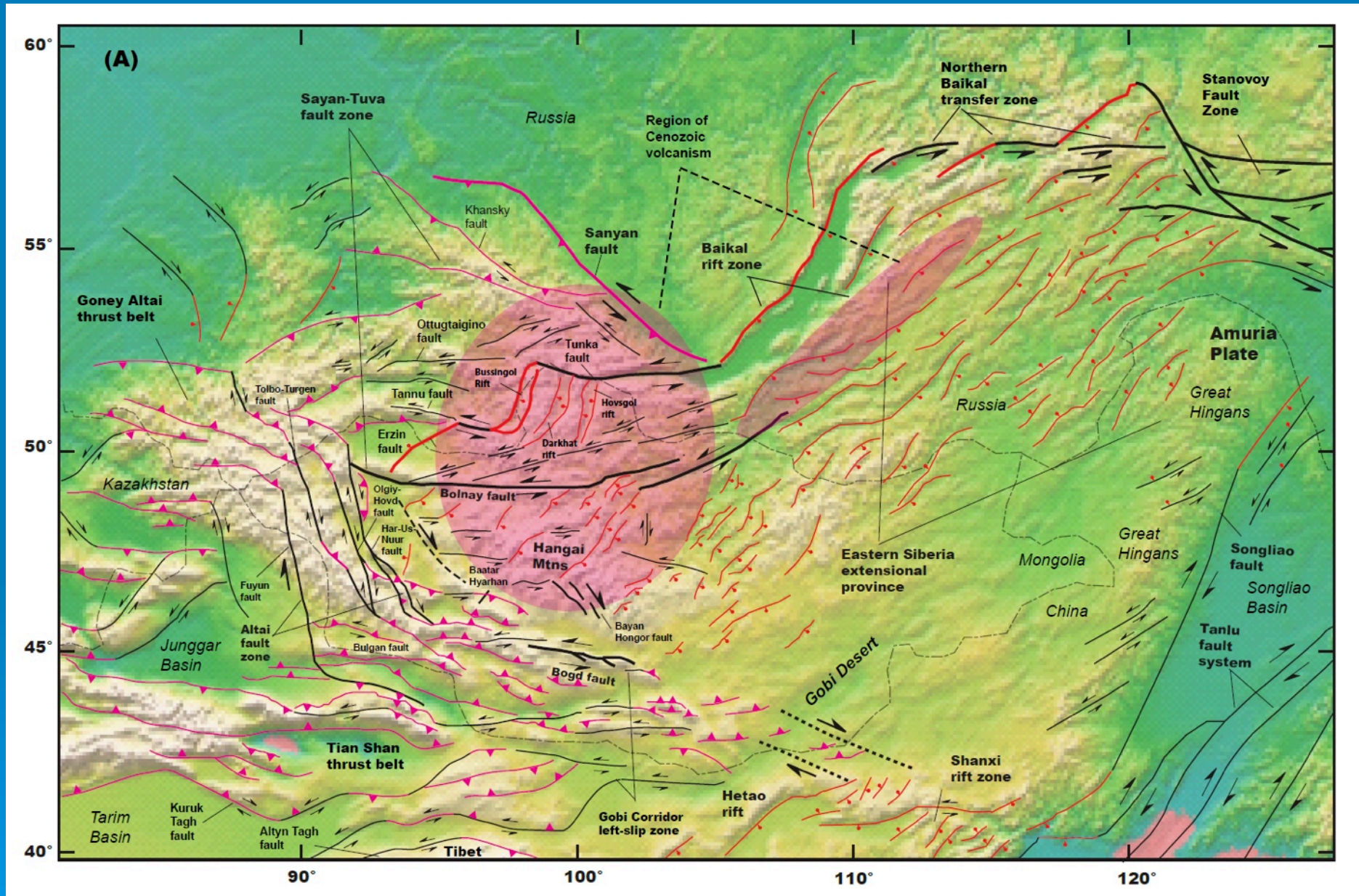
(A)
Sayan-Tuva fault zone
Russia
Region of Cenozoic volcanism
Northern Baikal transfer zone
Stanovoy Fault Zone
Khansky fault
Sanyan fault
Baikal rift zone
Goney Altai thrust belt
Ottugtaigino fault
Tunka fault
Bussingol Rift
Tolbo-Turgen fault
Tannu fault
Hovsgol rift
Erzin fault
Darkhat rift
Amuria Plate
Great Hingans
Russia
Kazakhstan
Olgiy-Hovd fault
Bolnay fault
Har-Us-Nuur fault
Hangai Mtns
Baatar Hyarhan
Eastern Siberia extensional province
Mongolia
Great Hingans
Songliao fault
Songliao Basin
China
Fuyun fault
Altai fault zone
Junggar Basin
Bayan Hongor fault
Bulgan fault
Tanlu fault system
Bogd fault
Gobi Desert
Tian Shan thrust belt
Shanxi rift zone
Hetao rift
Tarim Basin
Kuruk Tagh fault
Altyn Tagh fault
Gobi Corridor left-slip zone
Tibet
60°
55°
50°
45°
40°
90°
100°
110°
120°

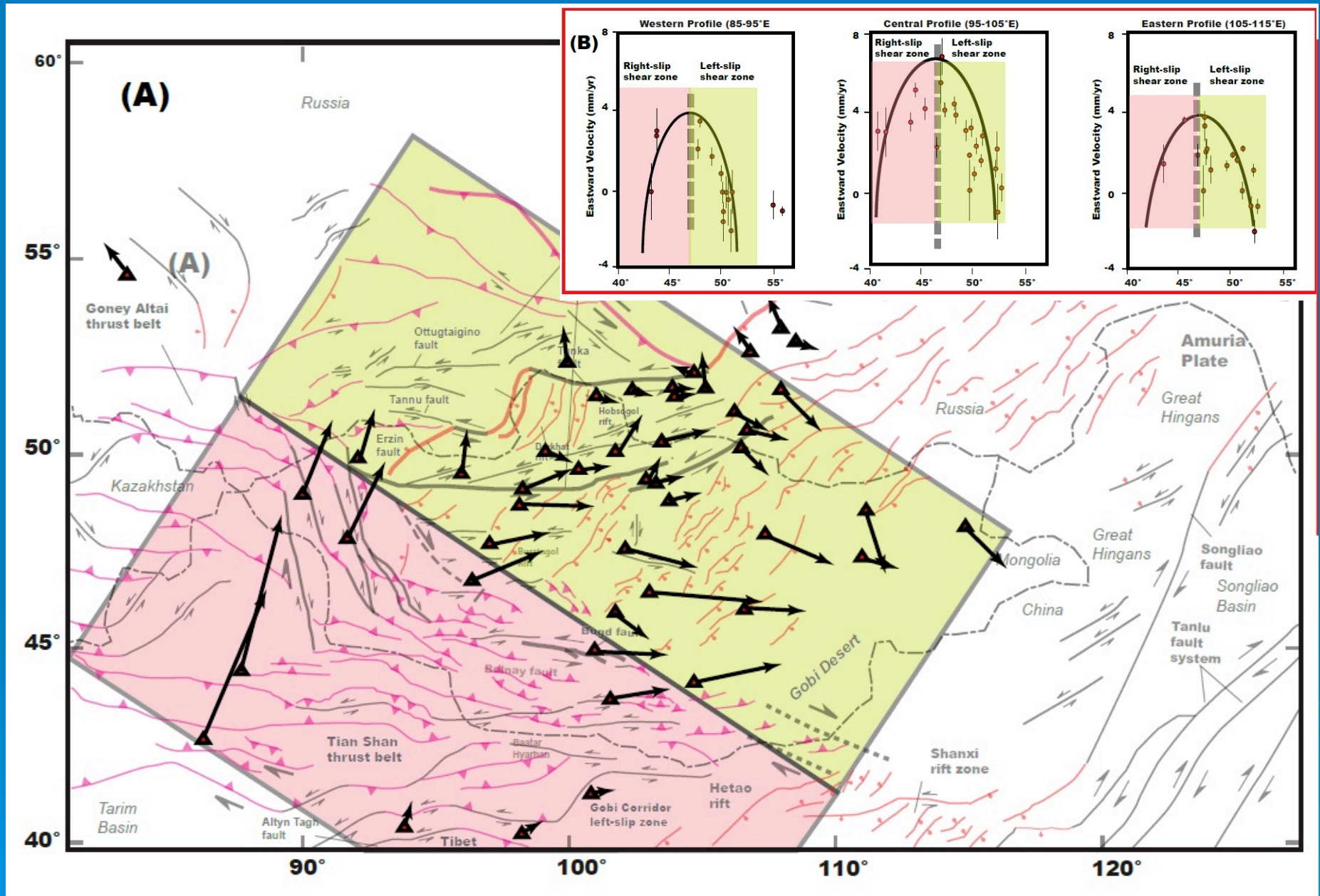
(A)
Russia
(A)
Goney Altai thrust belt
Ottugtaigino fault
Tannu fault
Erzin fault
Hobsogol rift
Kazakhstan
Bogd fault
Bolnay fault
Tian Shan thrust belt
Bastar Hyarhan
Tarim Basin
Altyn Tagh fault
Tibet
Gobi Corridor left-slip zone
Hetao rift
Gobi Desert
Shanxi rift zone
Amuria Plate
Great Hingans
Russia
Great Hingans
Songliao fault
Songliao Basin
Mongolia
China
Tanlu fault system
60°
55°
50°
45°
40°
90°
100°
110°
120°
(B)
Western Profile (85-95°E
Central Profile (95-105°E)
Eastern Profile (105-115°E)
Right-slip shear zone
Left-slip shear zone
Eastward Velocity (mm/yr)
8
4
0
-4
40°
45°
50°
55°

We can gain insight into the driving mechanism by examining our analytical form of GPS velocity field:

Velocity Field

$$u = \frac{S - U_0}{Lh^2} x(h^2 - 4y^2) + U_0$$

$$v = -\frac{V_0}{h} y$$

Strain-rate Field

$$\dot{\varepsilon}_{xx} = \frac{S - U_0}{Lh^2}(h^2 - 4y^2)$$

$$\dot{\varepsilon}_{yy} = -\frac{V_0}{h}$$

$$\dot{\varepsilon}_{xy} = -8\frac{S - U_0}{Lh^2} xy$$

Assume (1) conservation of mass and (2) horizontal velocity field does not vary with depth, we obtain vertical strain rate, velocity, basal shear, and pressure gradient

$$\dot{\varepsilon}_{zz} = \frac{\partial w}{\partial z} = -(\dot{\varepsilon}_{xx} + \dot{\varepsilon}_{yy}) = \frac{V_0}{h} - \frac{S - U_0}{Lh^2}(h^2 - 4y^2)$$

Strain rate

$$w = [\frac{V_0}{h} - \frac{S - U_0}{Lh^2}(h^2 - 4y^2)]z + f(x, y)$$

Vertical velocity

$$\frac{\partial \sigma_{zz}}{\partial z} + \frac{\partial \sigma_{zx}}{\partial x} + \frac{\partial \sigma_{zy}}{\partial y} - \rho g = 0$$

Stress equilibrium in vertical direction

1. Eastward basal shear at the base of the deforming layer in central Tibet:

$$\sigma_{xz} = \mu[(16\frac{U_0 - S}{Lh^2})x + c]$$

2. Eastward decrease in pressure gradient and lithospheric thickness:

$$\frac{\partial P}{\partial x} = -8\mu\frac{S - U_0}{Lh}x$$

$$H(x) = -\frac{12\mu(S - U_0)}{\rho g L h^2}x^2 + H_0$$

Thus, two possible driving mechanisms

- Shear at the base of Tibetan crust or lithosphere.
- Lateral gravitational spreading (thicker crustal region spreads to thinner crustal region).

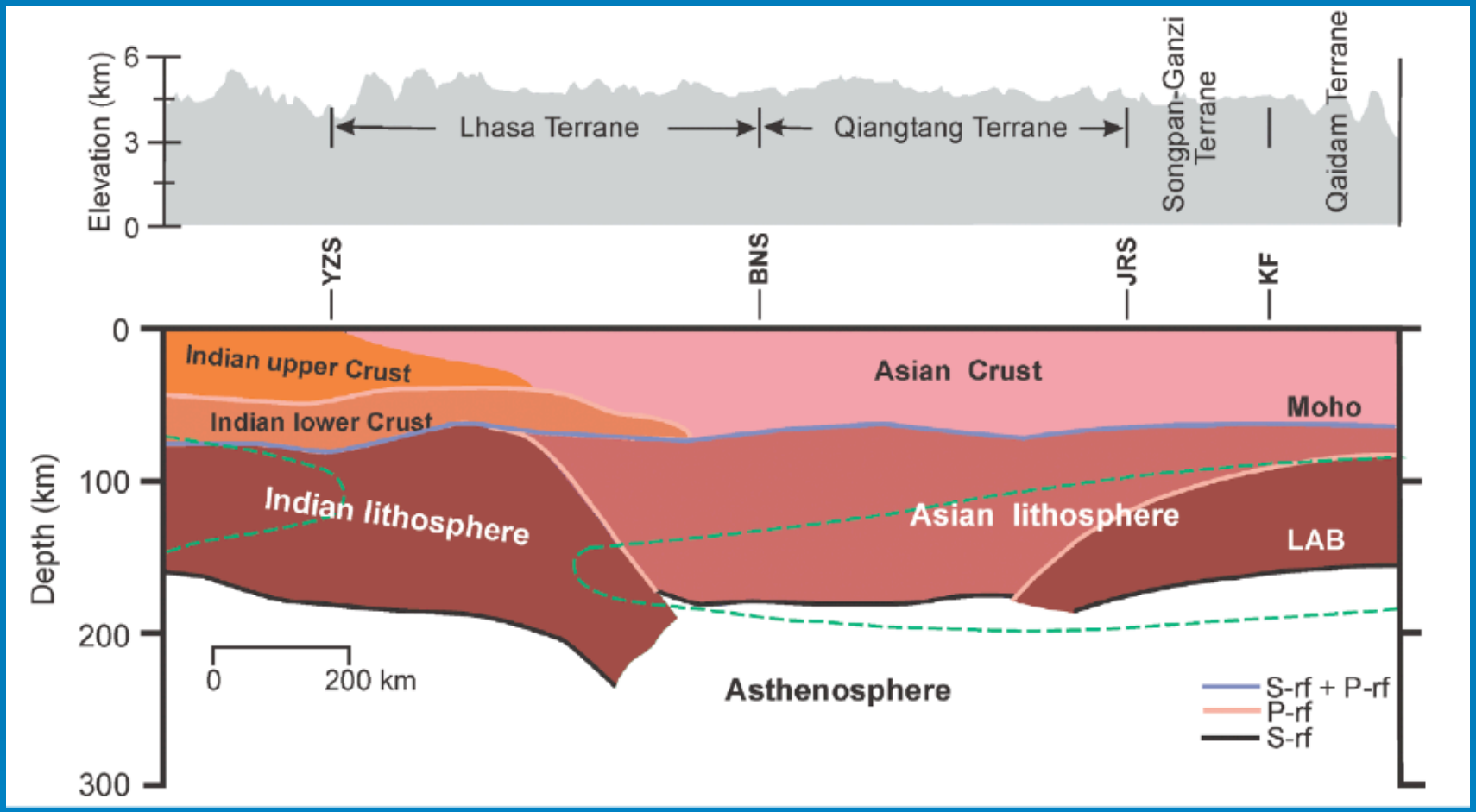

LAB: Lithosphere-Asthenosphere Boundary

Kumar et al. (2006)

Magnitude of seismic anisotropy consistent with H-P flow

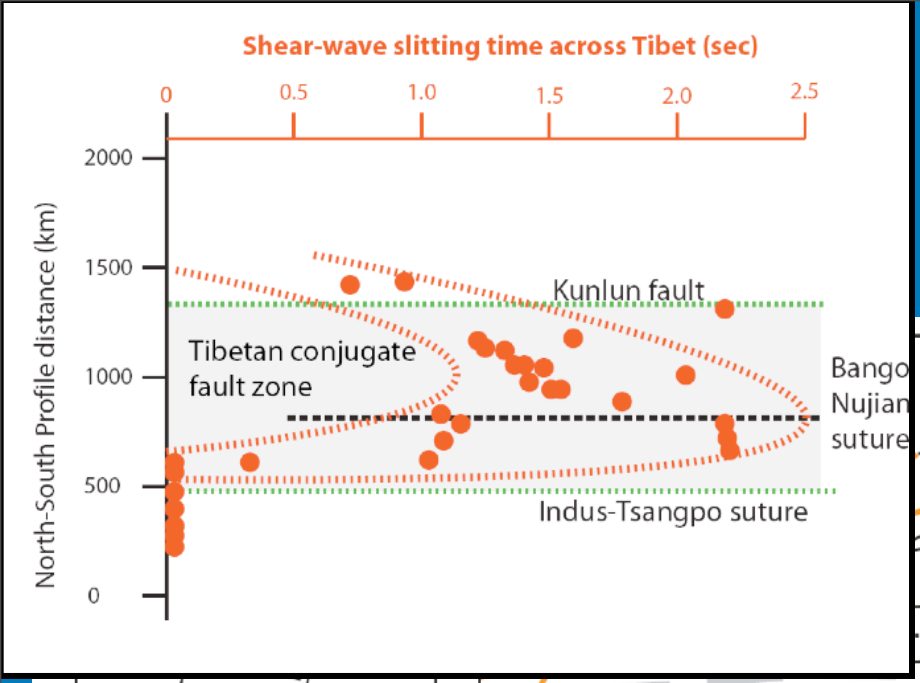

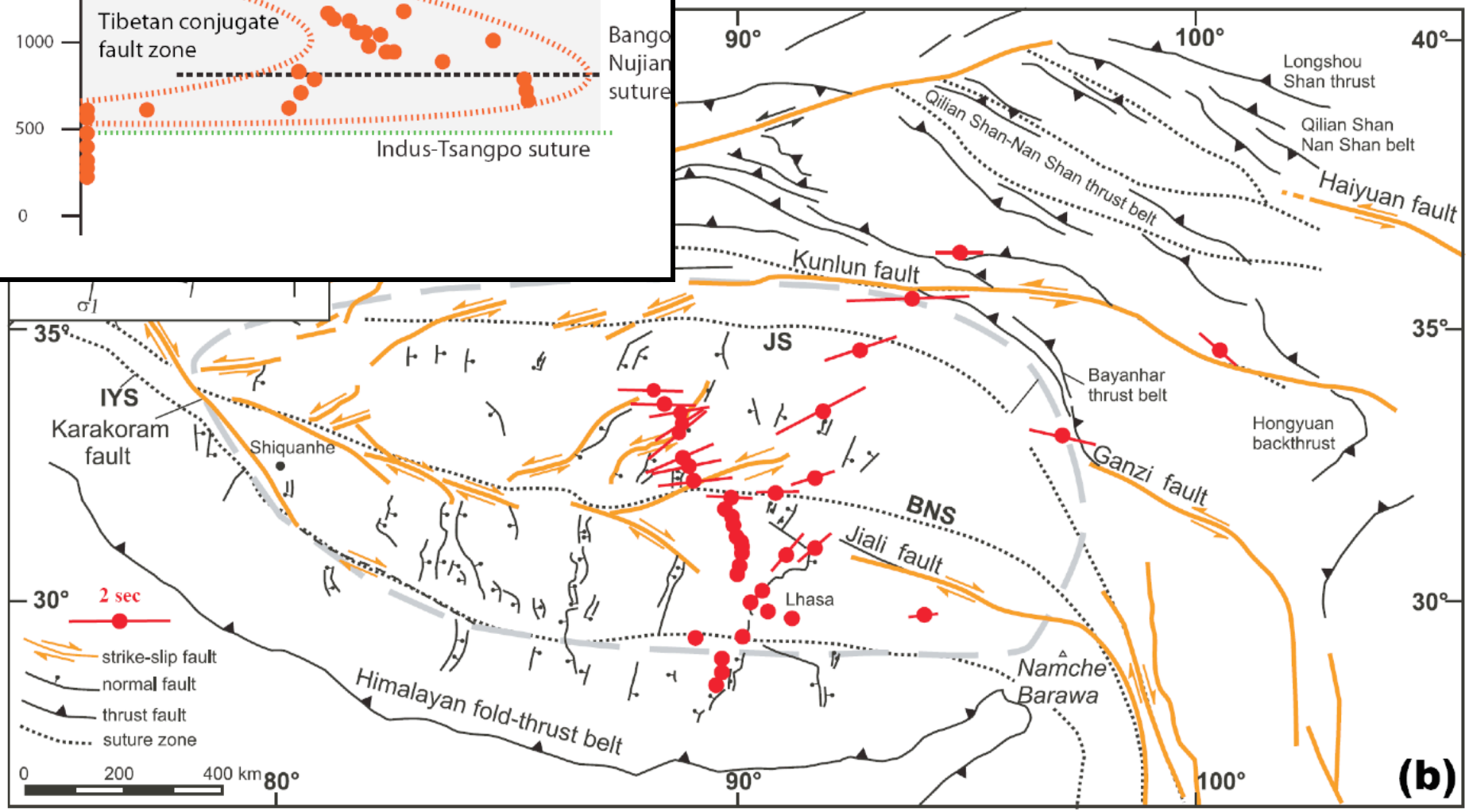

Seismic anisotropy compiled by Huang et al. (2000)

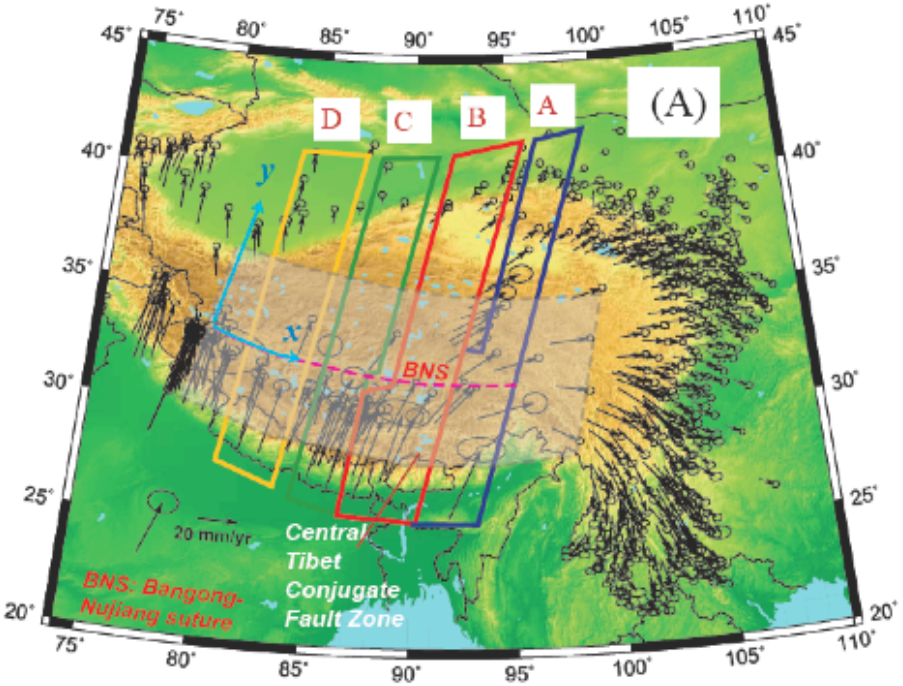
(A)
D
C
B
A
y
x
BNS
20 mm/yr
Central Tibet Conjugate Fault Zone
BNS: Bangong-Nujiang suture
75°
80°
85°
90°
95°
100°
105°
110°
45°
40°
35°
30°
25°
20°

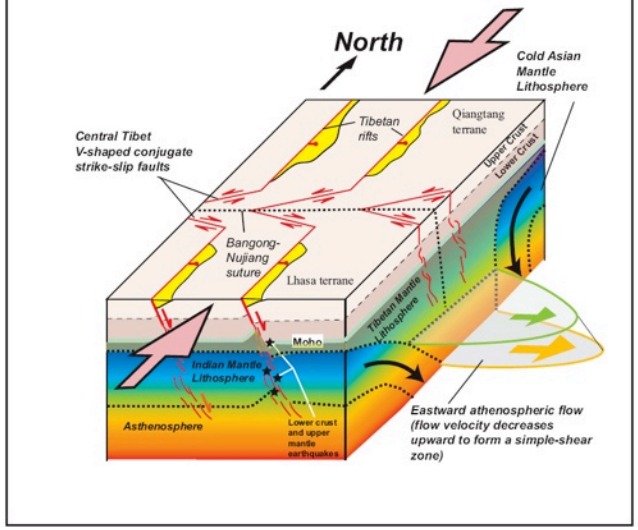
North
Cold Asian Mantle Lithosphere
Central Tibet V-shaped conjugate strike-slip faults
Tibetan rifts
Qiangtang terrane
Upper Crust
Lower Crust
Bangong-Nujiang suture
Lhasa terrane
Tibetan Mantle Lithosphere
Moho
Indian Mantle Lithosphere
Asthenosphere
Lower crust and upper mantle earthquakes
Eastward athenospheric flow (flow velocity decreases upward to form a simple-shear zone)

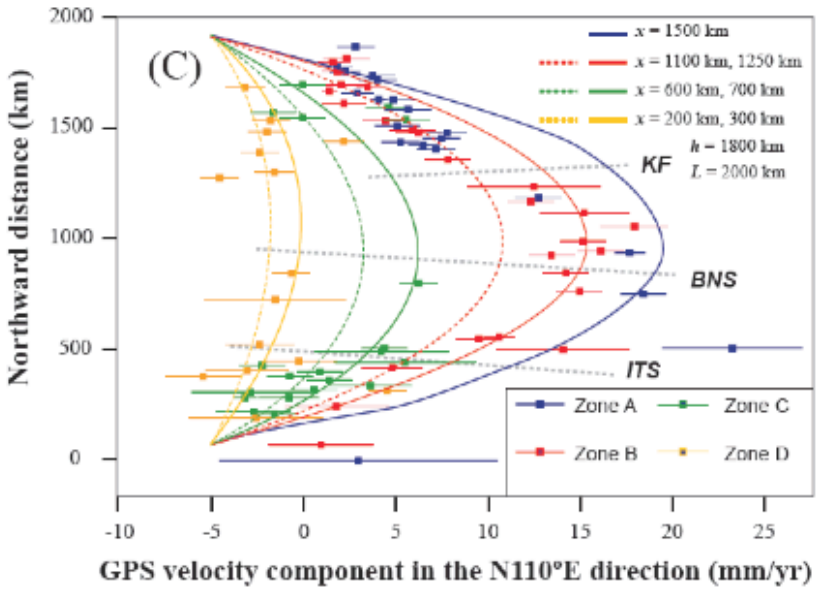
(C)
x = 1500 km
x = 1100 km, 1250 km
x = 600 km, 700 km
x = 200 km, 300 km
h = 1800 km
L = 2000 km
KF
BNS
ITS
Zone A
Zone C
Zone B
Zone D
Northward distance (km)
2000
1500
1000
500
0
-10
-5
0
5
10
15
20
25
GPS velocity component in the N110°E direction (mm/yr)

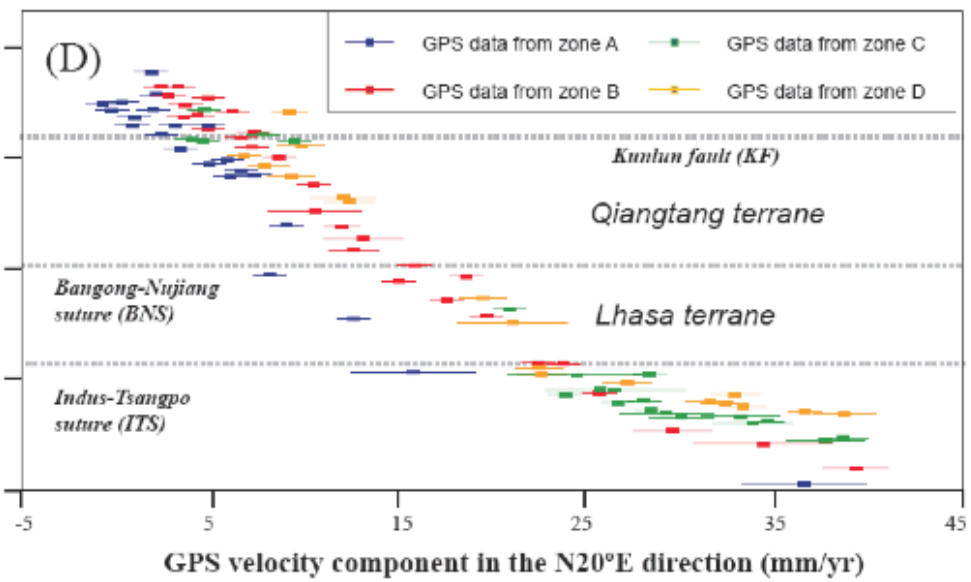
(D)
GPS data from zone A
GPS data from zone C
GPS data from zone B
GPS data from zone D
Kunlun fault (KF)
Qiangtang terrane
Bangong-Nujiang suture (BNS)
Lhasa terrane
Indus-Tsangpo suture (ITS)
-5
5
15
25
35
45
GPS velocity component in the N20°E direction (mm/yr)

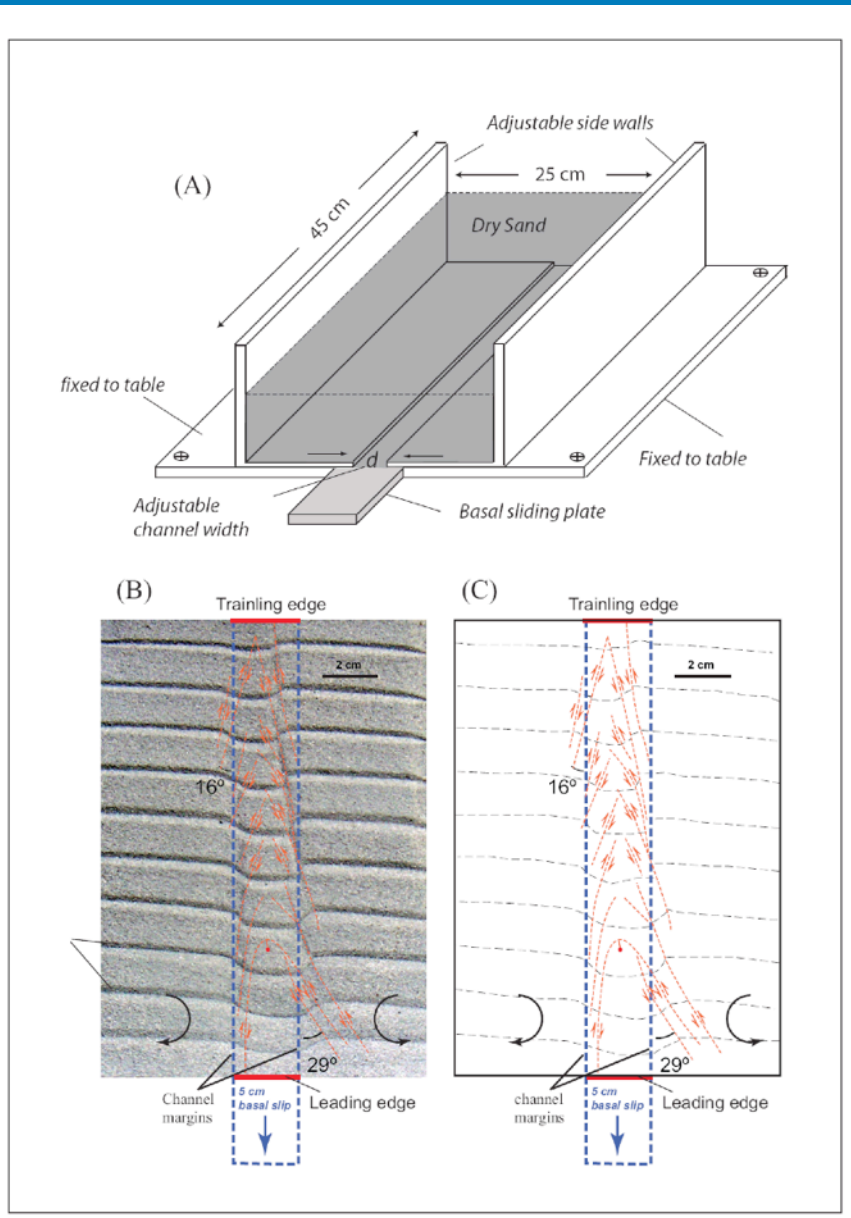
(A)
Adjustable side walls
25 cm
45 cm
Dry Sand
fixed to table
d
Fixed to table
Adjustable
channel width
Basal sliding plate
(B)
Trainling edge
2 cm
16°
29°
Channel
margins
5 cm
basal slip
Leading edge
(C)
Trainling edge
2 cm
16°
29°
channel
margins
5 cm
basal slip
Leading edge

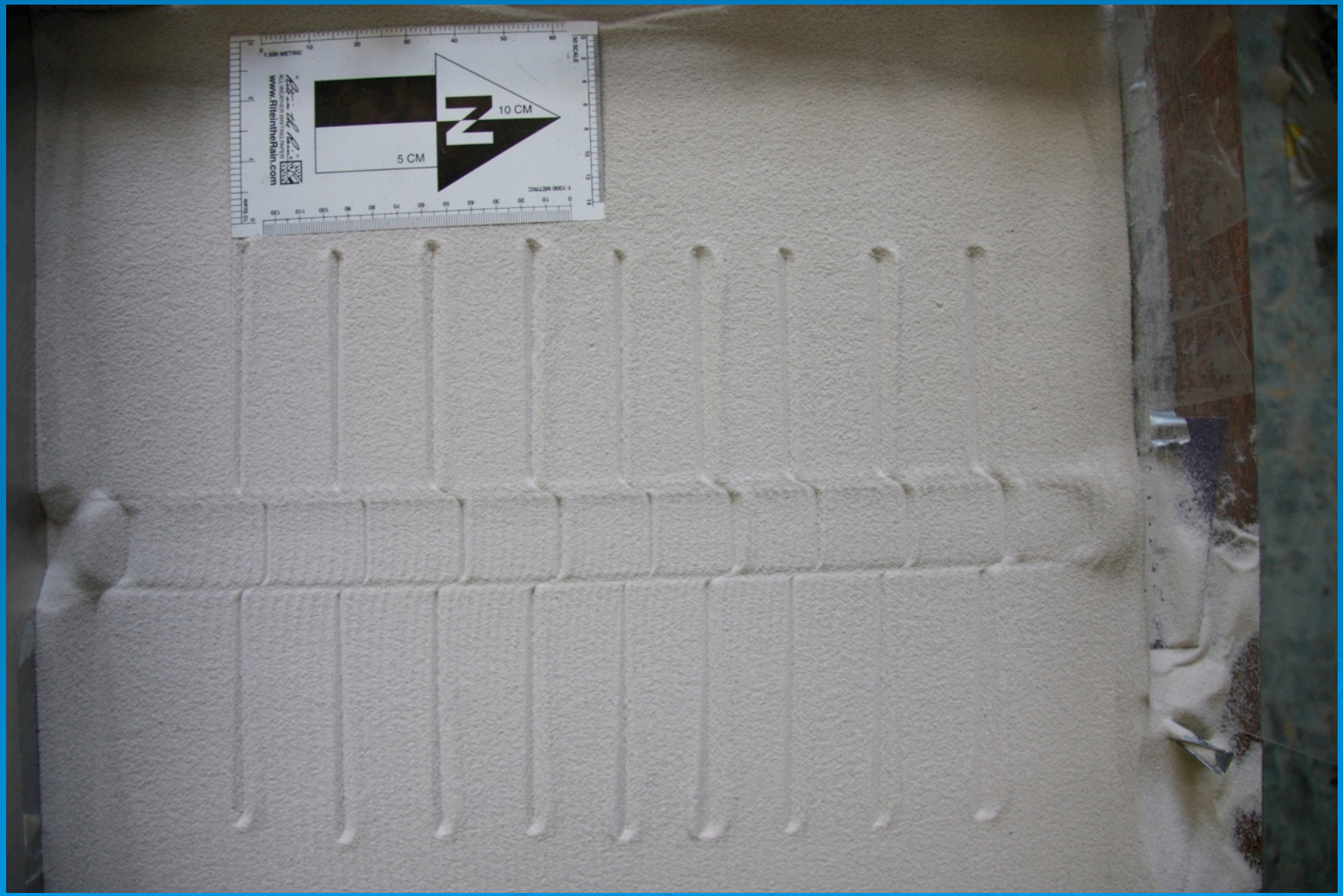
10 CM
5 CM
www.RiteintheRain.com


10 CM
34 mm

Is orientation of fault formation controlled by state of strain?

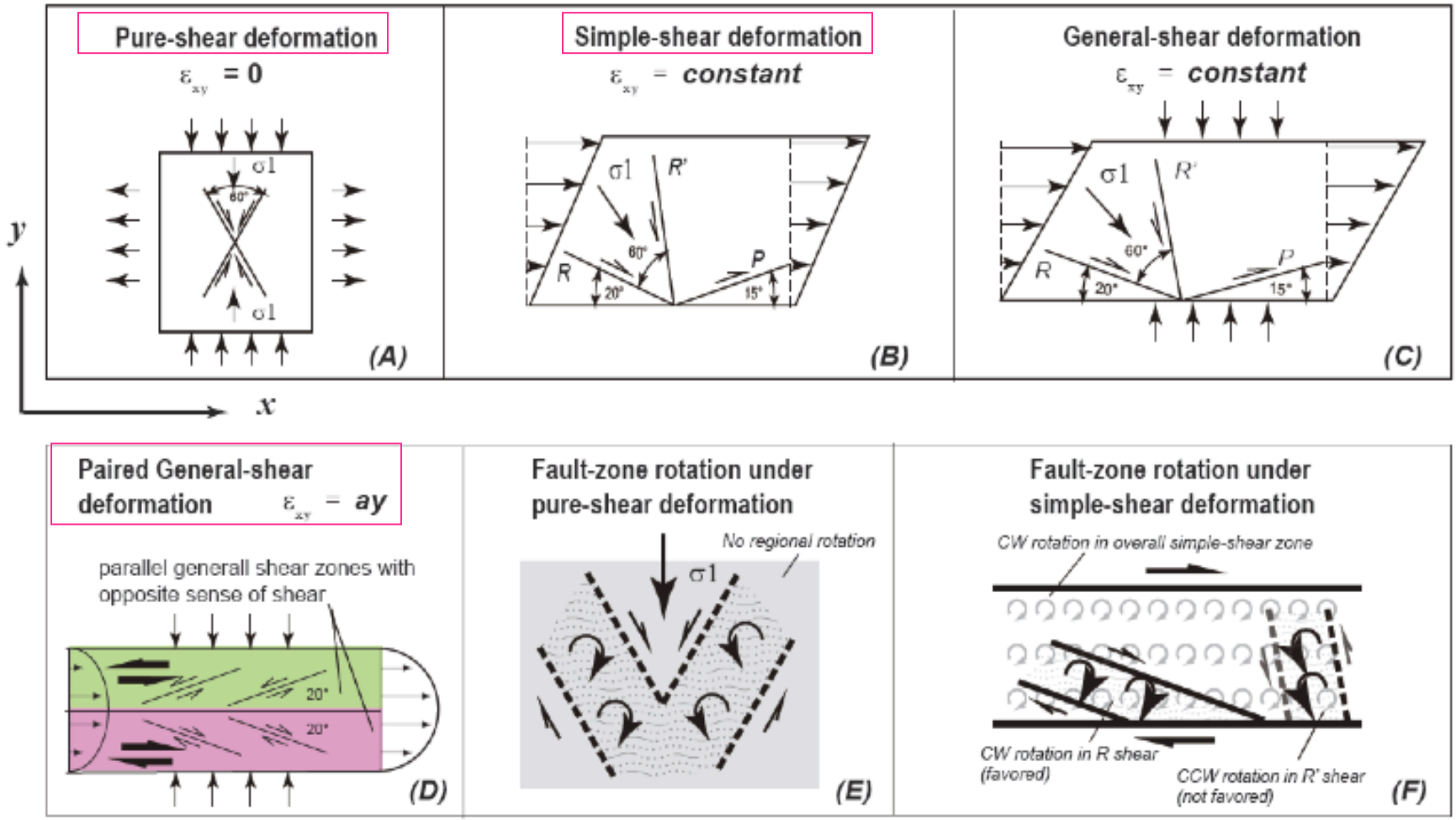

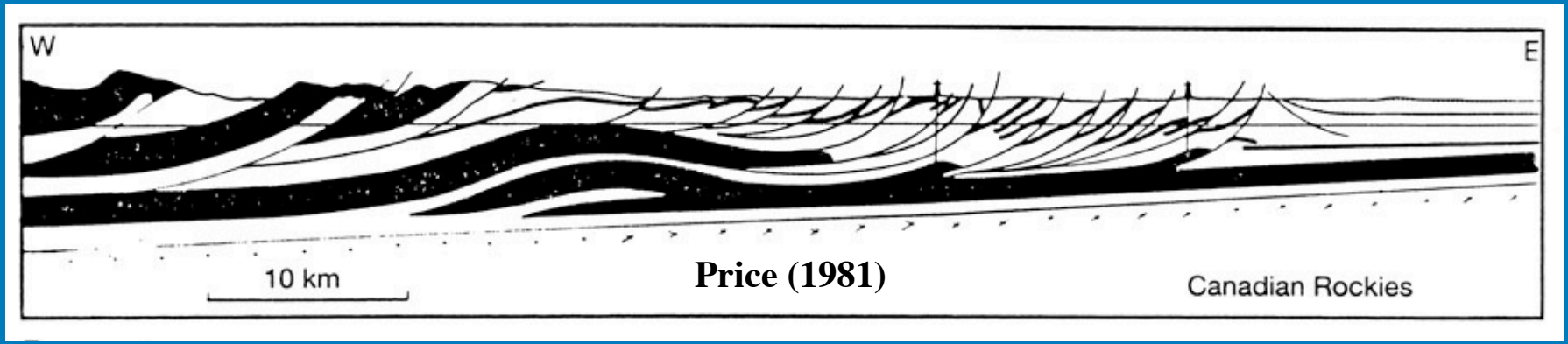

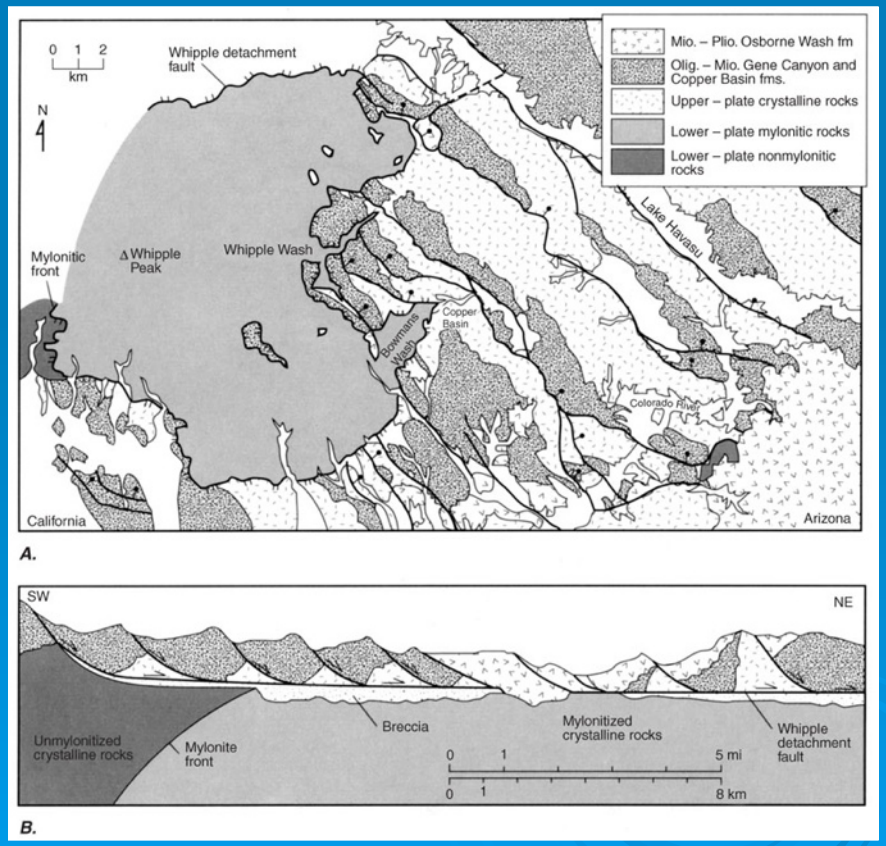

Whipple Detachment System

Davis (1981)

If strain/strain rate controls orientation of fault formation, we can also explain other odd faults

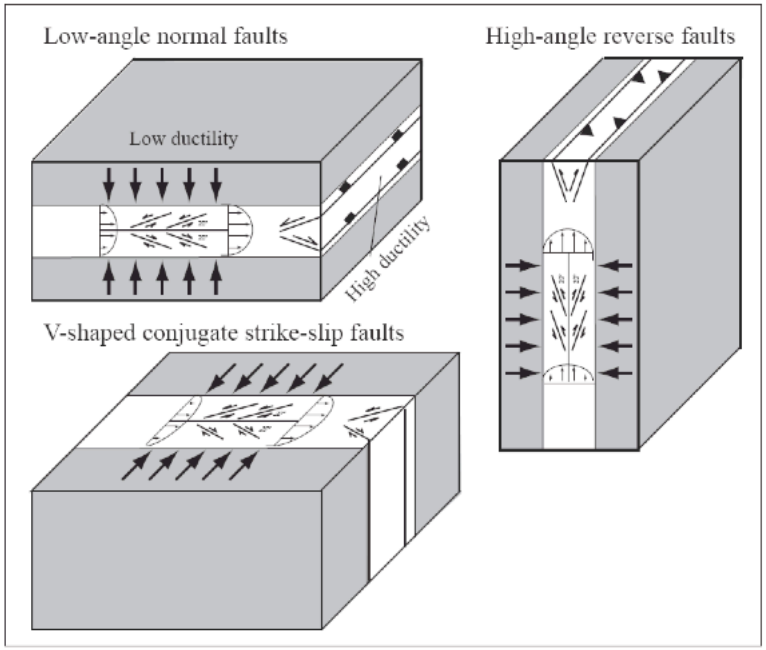

Strain controlled fault formation pattern

Anderson fault classification

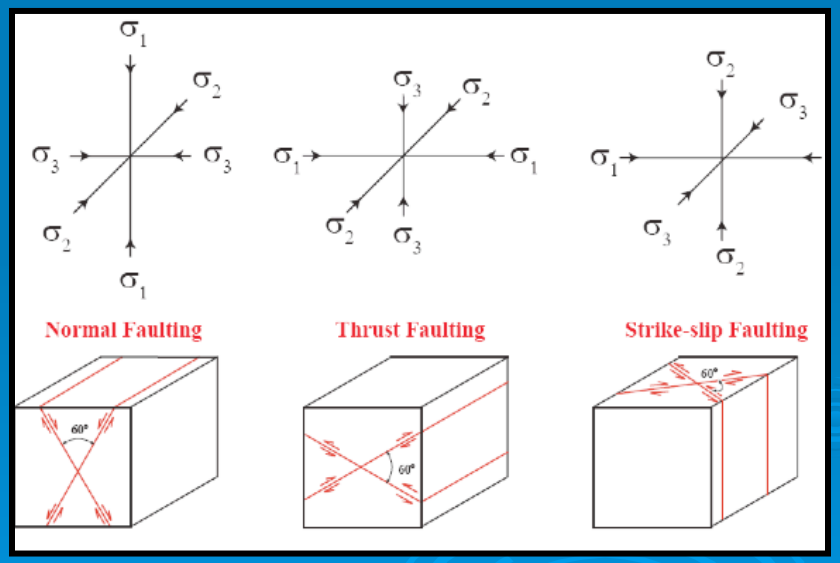

Stress controlled fault formation pattern

Testing the two continental-deformation models:

Micro-plate Model (also known as the "extrusion model"): ***A few large faults with fast slip rates bounding little deformed continental blocks.***

Thin Viscous Sheet Model (also known as the "distributed deformation model"): ***All faults were created equal, each having small displacement and slow slip rates. Overall deformation field can be approximated by viscous flow.***

Flow is not only a convenient way of describing large parts of continental deformation, but is required for the formation of a widely distributed odd fault systems that we termed V-shaped conjugate strike-slip faults. This new understanding also requires reevaluation of the fault-initiation mechanisms.

Whipple Detachment Fault System

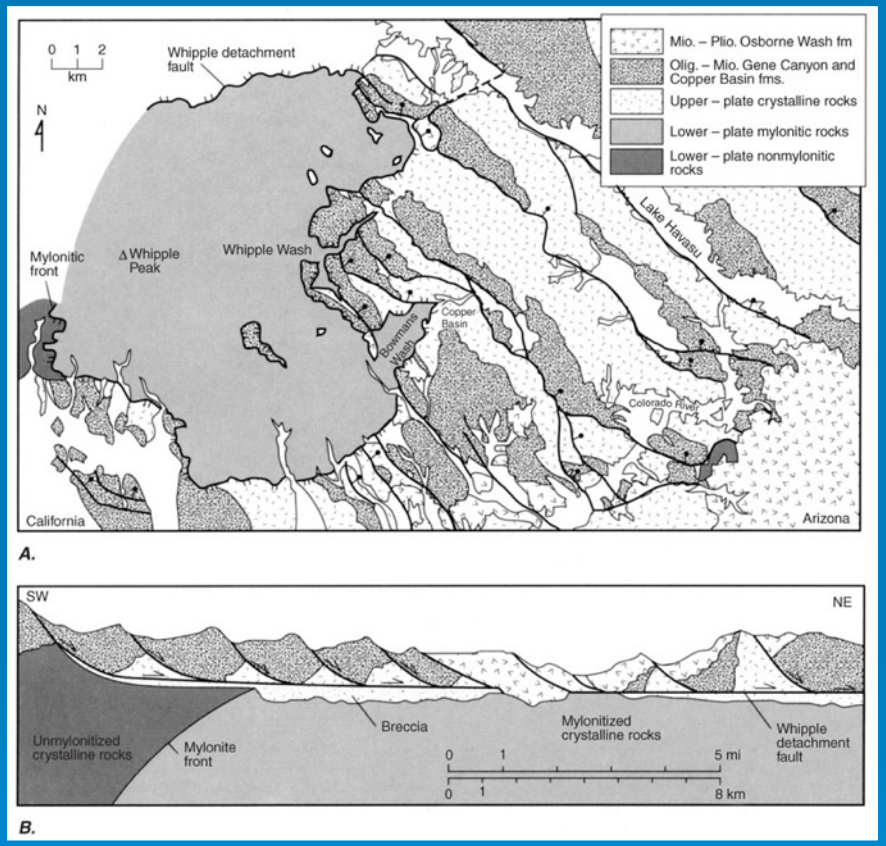

Figure 5.13 Faulting in the Whipple Mountain metamorphic core complex of the Basin and Range province, southeastern California. *A*. Map of the Whipple Mountains metamorphic core complex. *B*. Diagrammatic cross section through the Whipple Mountains before uplift domed the detachment fault. *C*. The Whipple Mountain detachment fault (arrow) is marked by a topographic ledge of cataclastic rocks (see Figure 4.5*B*) along which the dark-colored tilted Tertiary strata are faulted against the underlying, lighter-colored mylonitic gneisses.

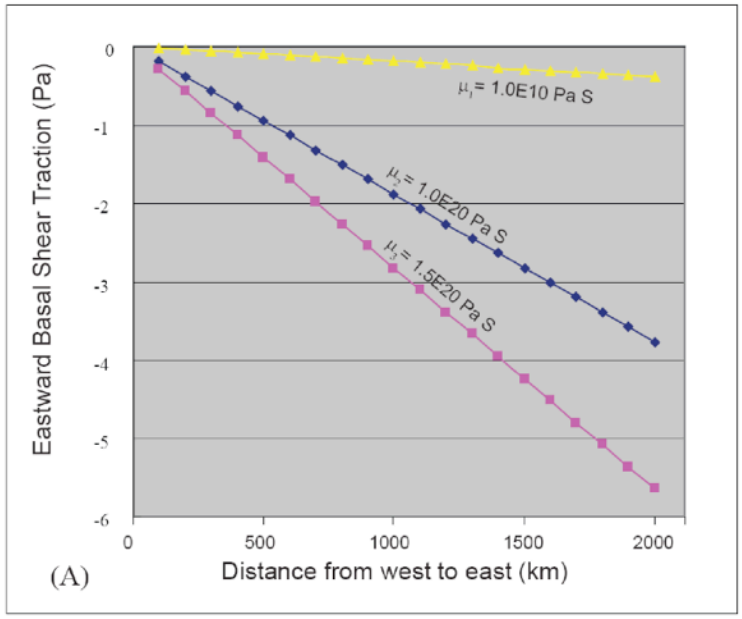

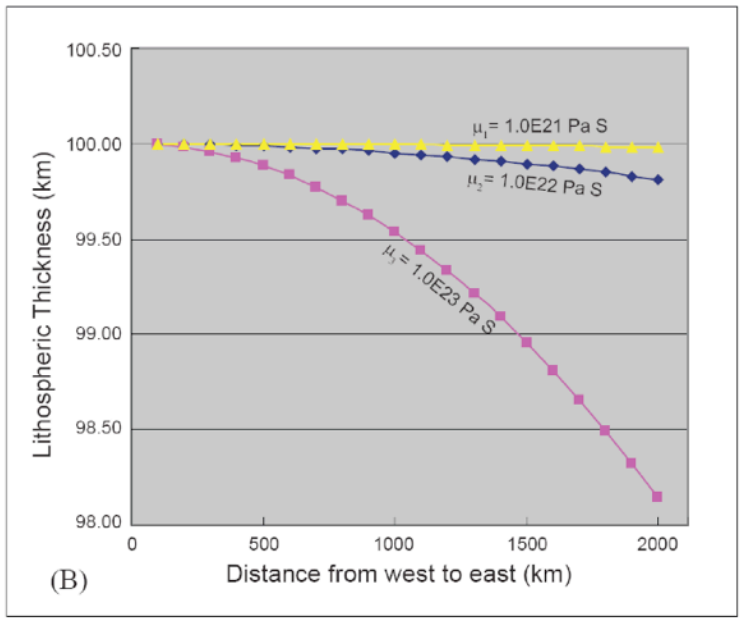

1. Eastward variation of basal shear traction as a function of viscosity.

1. Eastward variation of lithospheric thickness as a function of viscosity.